An Efficient Pose Measurement Method of a Space Non-Cooperative Target Based on Stereo Vision

JIANQING PENG[ID][1]**, WENFU XU**[1,2]**, (Senior Member, IEEE), AND HAN YUAN**[1]

[1]School of Mechanical Engineering and Automation, Harbin Institute of Technology, Shenzhen 518055, China
[2]State Key Laboratory of Robotics and System, Harbin Institute of Technology, Harbin 150001, China

Corresponding author: Han Yuan (yuanhan@hit.edu.cn)

ABSTRACT Pose (position and attitude) measurement of a space non-cooperative target is very important for on-orbital servicing tasks, including malfunctioning target repairing, space debris removal, and so on. However, such targets are generally non-cooperative, i.e., no markers are mounted on it and there is no prior knowledge. Therefore, the identification and measurement of a non-cooperative target is very challenging. In this paper, we propose an efficient method to recognize the natural objects with circular or near-circular shapes on the target, reducing the computation load and improving accuracy. First, the geometry properties of a practical non-cooperative target are analyzed. A stereo vision system is correspondingly designed to measure the relative pose of the target. Second, the error sources and time-consuming factors of the traditional method are analyzed. Then, a solution concept is proposed. Third, the efficient method is detailed to solve the geometry equation and determine the pose information, reducing the calculation complexity and increasing the accuracy. The image pre-processing and target detecting algorithms are realized on FPGAs, further accelerating the calculation speed. Finally, we develop an experiment system and verify the proposed method through practical experiments. The experiment system is composed of satellite mockup, binocular camera, and high precision laser tracker. The experiment results show that the proposed method has high accuracy and efficiency.

INDEX TERMS Non-cooperative targets, pose measurement, stereo vision system, on-orbital servicing, FPGAs.

I. INTRODUCTION

With the continuous exploration of space technology, a large number of man-made objects are constantly being launched into space, resulting in an increase of space debris, including abandoned satellites, rocket bodies, and other un-controlled objects. The space debris not only occupies the valuable orbit resources, but also seriously affects operational satellites. According to the ESA forecast, if there are no effective measures to remove space debris, by 2030 or so, there will be a 3.7% probability of collision. That is to say, every 25 normal satellites will have one potential collision with the uncontrolled object. Therefore, protecting valuable and limited orbit resources becomes broad consensus in the international community [1], [2].

Recently, the on-orbital servicing technology based on space robots is proposed to capture and remove the space debris [3], [4]. The target recognition and pose measurement are the keys to space debris disposal [5]. According to the orbital dynamics, a space un-controlled object is generally in a tumbling state. Moreover, there is not any measurement marker or handle mounted on the target. That is to say, such targets are non-cooperative and tumbling. Therefore, it is very challenging to recognize and measure them.

Identification and measurement of non-cooperation target is a worldwide problem, which has attracted lots of attentions from engineers and scholars. ESA(European Space Agency) designed a geostationary orbit restorer to capture abandoned satellites in orbit [6]. The laser ranging and active vision

measures were used. Thienel *et al.* [7] proposed a nonlinear approach to estimate the spacecraft attitude for the service of the Hubble Space Telescope and conducted tracking control under the auspices of NASA. But it needed more priori knowledge. Du *et al.* [8] proposed a pose measurement method for large un-controlled satellites in orbit using collaborative cameras. But the geometry was assumed to be known. Zhang *et al.* [9] proposed a pose measurement method without the use of cooperative cursors, but assuming that the shape and geometry of the identified target were known. Inaba *et al.* [10] proposed a method for on-orbit identification and capture of non-cooperative targets, but assuming that the shape, size and quality of the target were known. Lichter and Dubowsky [11] proposed a method of estimating the target state, geometry, and model parameters, but this method required a number of three-dimensional visual sensors in different directions for the target shooting, causing high cost and operational burden to the space task. Jasiobedski *et al.* [12] proposed a stereo–vision-camera-based vision system that allows pose measurement and tracking in the proximity of satellites. Terui *et al.* [13] also studied the use of stereo vision to estimate the motion of the failed satellite. Gao *et al.* [14] proposed an algorithm for measuring the unknown position and attitude of unknown dimensions using a monocular camera and a laser range finder, but there was also a problem that the monocular camera cannot obtain a large-sized target image at close range. NASA designed a capture mechanism for non-cooperative target orbit engines, and presented a complex non-cooperative target recognition algorithm based on multi-sensor data fusion [15], [16]. This method could be affected by transmission delay and transmission reliability, when the delay was large, the entire system would be unstable. The United States carried out the FREND project mainly for non-cooperative spacecraft to perform capture, derailment and other operations [17], [18]. It used three hand-eye cameras as the pose measurement system [19].

There also have been some achievements in the measurement of non-cooperative tumbling targets. Li *et al.* [20] proposed a relative attitude estimation method based on parallel binocular non-cooperative spacecraft, which achieved the attitude measurement of satellite triangular support. Zhang *et al.* [21] proposed a new method for relative attitude and position estimation of tumbling spacecraft. This method could release the assumption that the main frame of the traditional algorithm coincides with its LVLH frame. The equation of the eccentric orbital motion was used to describe the position dynamics. The relative quaternion, the relative position and velocity, the subrographic deviation, and the principal angular velocity and inertia ratio could be estimated by the extended kalman filter. Sun *et al.* [22] studied the relative position and attitude tracking method in the case of model uncertainties and external disturbances when non-cooperative spacecraft were returned. Considering the difficulty of aligning the propeller in the process of tracking the spacecraft, a comprehensive robust adaptive controller with 6DOF relative motion was designed. The gradient uncertainty

of the tracker was estimated by the gradient adaptive method. Lyapunov theory was used to prove that the error of the closed loop system was asymptotically converted to zero. Tweddle [23] proposed a new method to solve simultaneous localization and mapping problems by estimating the position of the target, the method used an incremental smoothing and mapping system to examining unknown non-cooperative targets that revolve around any axis in the space, direction, line speed, angular velocity, centroid, spindle and inertia ratio. However, this method was too computationally intensive and was not suitable for the study of real-time capture system for space robots. Dong *et al.* [24] used the extended kalman filter to develop a real-time attitude and motion estimation method for non-cooperative targets. The optical flow algorithm tracked the feature points of the target and improved the image processing speed. The scheme was implemented the attitude and motion estimation of dynamic target by a single camera. Kaiser *et al.* [25] proposed an optimization algorithm for the integration of inertial sensors and vision sensors for pose measurement, and successfully realized the pose measurement and motion prediction for four quadrotor MAV. Dong *et al.* [26] also developed a motion-based controller that performs automatic capture of non-cooperative targets. In order to accurately estimate the movement of the target, the camera vision measurement and the kalman filter combination method ensure the accuracy of target state prediction.

In this paper, we focus on measuring the geometrical shape and pose of the non-cooperative target to determine the appropriate capture position for the space robot. In order to solve the problem of large computational complexity and low accuracy, an efficient solution for solving the pose of natural objects with circular or near-circular shape is deduced in detail. The eigenvalues and eigenvectors of the oblique cone are analyzed from the essence of space circle imaging. Aiming at the space non-cooperative target, the accurate pose information is obtained by binocular collaborative measurement. The validity of the algorithm is verified by experiments.

The remainder of this paper is organized as follows. A stereo-vision-based pose measurement system is designed in Section II. The traditional pose calculation method is introduced in Section III and then an efficient solving concept with high accuracy is proposed. In Section IV, the detailed solution method based on stereo-vision collaborative measurement is proposed. The parallel computing idea for image pre-processing of pose measurement is realized on FPGAs. In Section V, an experimental system of binocular stereoscopic vision is established and the validity of the method is verified through experiments. The last section presents the summary and conclusions.

II. DESIGN OF A NON-COOPERATIVE MEASUREMENT SYSTEM BASED ON STEREO VISION
A. NON-COOPERATIVE SATELLITE MODEL
The non-cooperative target that we want to be serviced is assumed to be a malfunctioned satellite, named *Xinnuo*-2.

The satellite has two solar wings, which are mounted on the $+Y$ and $-Y$ panels respectively, and two large antennas on the $+X$ and $-X$ panels. When the *Xinnuo*-2 satellite reaches the GEO orbit successfully, some accidents happened, as shown in Fig. 1, and some mechanical parts have not been unfolded, such as:
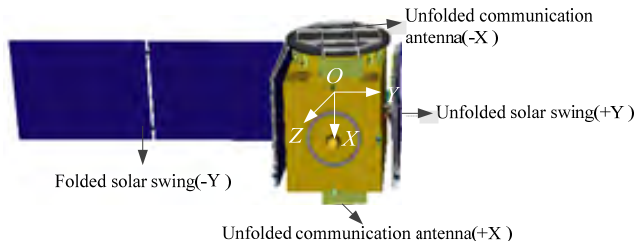

FIGURE 1. The malfunctioned *Xinnuo*-2 satellite to be repaired.

(i)   The $+Y$ solar wing fails to be unfolded;
(ii) The $+X$ communication antenna fails to be unfolded;
(iii) The $-X$ communication antenna fails to be unfolded.

To ensure the normal operation of the communication satellite, theses unfold mechanical parts must be repaired. The following sections will provide a solution for on-orbit services.

B. DESIGN OF THE STEREO VISION SYSTEM

In order to carry out pose measurement for non-cooperative target, a binocular stereo vision system is designed. As shown in Fig. 2, since the launch vehicle interface ring and apogee engine nozzle are mounted on nearly all the GEO satellites, so it is a good choice to take them as the recognition objects.
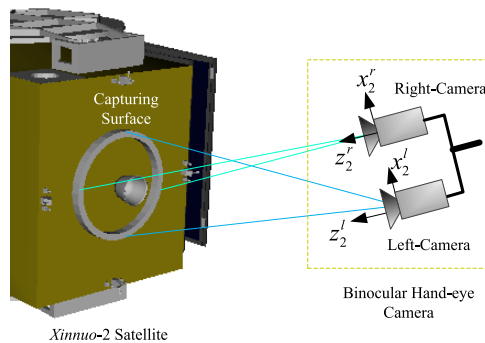

FIGURE 2. The feature recognition based on stereo vision system.

As we can see, the apogee engine nozzle has circular or near-circular shapes. A circular shape is an ideal choice due to the following properties:

(i)   A circle can be defined with only three parameters (i.e. x_0, y_0, r), and its perspective projection in any arbitrary orientation is a standard ellipse;
(ii) A circle has a better visual positioning accuracy;
(iii) The complete boundary or an arc of a projected circular feature can be used for pose estimation without knowing the exact point correspondence.

Here, by taking the natural circular features on the target as the recognized objects, we propose a binocular stereo-vision-based method to estimate the surface normal of the capturing plane and the center position of the circle. The definition of each coordinate system is shown in Fig. 3, where:
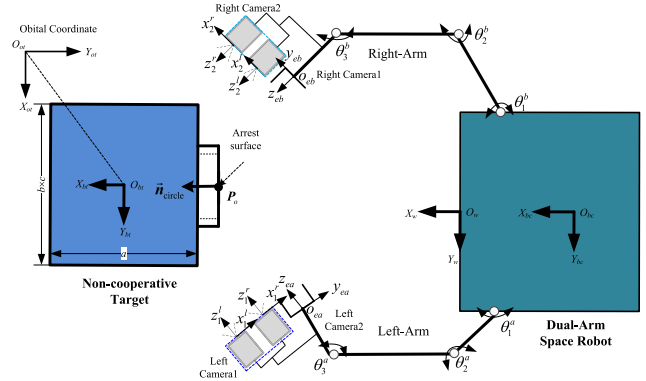

FIGURE 3. The schematic diagram of stereo vision measurement system.

$O_{ot} - X_{ot}Y_{ot}Z_{ot}$ is the orbital coordinate system of the space target; it is used as the global reference frame for the dynamic modeling; its origin is the centroid of the target, x-axis is the flying direction and z-axis points to the center of the earth;

$O_{bc} - X_{bc}Y_{bc}Z_{bc}$, $O_{bt} - X_{bc}Y_{bt}Z_{bt}$ are the geometry reference frames of space robot base and non-cooperative target, respectively;

$O_L - X_LY_LZ_L$, $O_R - X_RY_RZ_R$ are the left and right camera coordinate system, whose origin is the optical center of corresponding camera;

$O_W - X_WY_WZ_W$ is the world frame, it is used as the capturing reference frame.
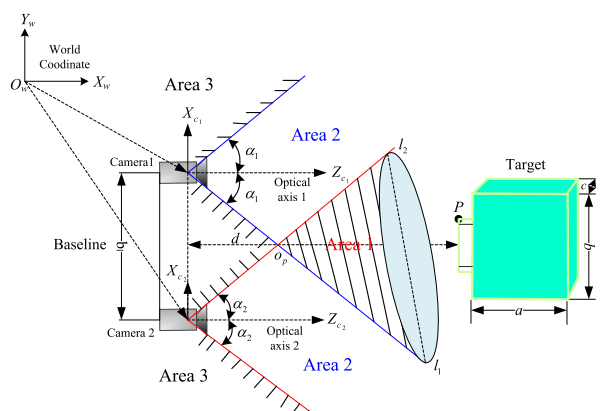

FIGURE 4. Observation range of binocular stereo vision system.

As shown in Fig. 4, area 1 is the three-dimensional imaging region and the two cameras can observe the target; area 2 is the camera half dead zone, only one camera can be observed; area 3 is the camera dead zone, the two cameras cannot observe the target.

According to stereoscopic knowledge, we can get the coordinate of the critical point o_p:

$$\begin{cases} x_{o_p} = X_{c_1} - \dfrac{b_l \cos \alpha_2 \sin \alpha_1}{\sin (\alpha_1 + \alpha_2)} \\[2mm] y_{o_p} = Y_{c_1} \\[2mm] z_{o_p} = Z_{c_1} + \dfrac{b_l \cos^2 \alpha_1}{\sin (\alpha_1 + \alpha_2)} \end{cases} \tag{1}$$

It means that the effective measurement area is a pyramidal frustum, among them, the vertex point is o_p, and the two generatrice are l_1 and l_2, respectively.

In the effective area, the two cameras simultaneously observe the target and extract the same feature point P. Assuming that the three-dimensional coordinates of the point P is (X, Y, Z), the image coordinates of the left and right cameras imaging plane are $p_l (u_l, v_l)$ and $p_r (u_r, v_r)$, respectively. p_l and p_r are the image in the world space, as shown in Fig. 5.
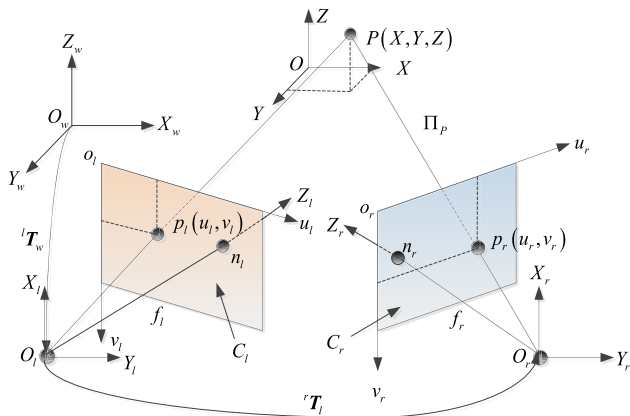

FIGURE 5. The schematic diagram of binocular 3-D reconstruction.

Assuming that the homogeneous transformation matrix of the left camera coordinate system relative to the world coordinate system $O_w - X_w Y_w Z_w$ is ${}^l\boldsymbol{T}_w$, the left and right camera's image coordinate system are set to $O_l - X_l Y_l Z_l$ and $O_r - X_r Y_r Z_r$, respectively; the corresponding effective focal length are f_l and f_r, respectively; the coordinates of the target point P in the left and right camera coordinate systems are (x_l, y_l, z_l) and (x_r, y_r, z_r), respectively. According to the perspective projection transformation model, we can obtain:

$$s_l \begin{bmatrix} X_l \\ Y_l \\ 1 \end{bmatrix} = \begin{bmatrix} f_l & 0 & 0 \\ 0 & f_l & 0 \\ 0 & 0 & 1 \end{bmatrix} \begin{bmatrix} x_l \\ y_l \\ z_l \end{bmatrix} \tag{2}$$

$$s_r \begin{bmatrix} X_r \\ Y_r \\ 1 \end{bmatrix} = \begin{bmatrix} f_r & 0 & 0 \\ 0 & f_r & 0 \\ 0 & 0 & 1 \end{bmatrix} \begin{bmatrix} x_r \\ y_r \\ z_r \end{bmatrix} \tag{3}$$

The homogeneous transformation matrix ${}^r\boldsymbol{T}_l$ between the left camera coordinate system $O_l - X_l Y_l Z_l$ and the right

camera coordinate system $O_r - X_r Y_r Z_r$ can be expressed as:

$$\begin{bmatrix} x_r \\ y_r \\ z_r \\ 1 \end{bmatrix} = {}^r\boldsymbol{T}_l \begin{bmatrix} x_l \\ y_l \\ z_l \\ 1 \end{bmatrix} = \begin{bmatrix} {}^r\boldsymbol{R}_l & {}^r\boldsymbol{t}_l \\ O^{\mathrm{T}} & 1 \end{bmatrix} \begin{bmatrix} x_l \\ y_l \\ z_l \\ 1 \end{bmatrix}$$

$$= \begin{bmatrix} r_{11} & r_{12} & r_{13} & t_x \\ r_{21} & r_{22} & r_{23} & t_y \\ r_{31} & r_{32} & r_{33} & t_z \\ 0 & 0 & 0 & 1 \end{bmatrix} \begin{bmatrix} x_l \\ y_l \\ z_l \\ 1 \end{bmatrix} \tag{4}$$

Among them, ${}^r\boldsymbol{R}_l$, ${}^r\boldsymbol{t}_l$ are the left and right camera attitude transformation matrix and translation vector, respectively.

Simultaneous (2), (3) and (4), the coordinates of the target point $\boldsymbol{P}$ can be introduced by

$$\begin{cases} X = Z \dfrac{X_l}{f_l} \\[3mm] Y = Z \dfrac{Y_l}{f_l} \\[3mm] Z = \dfrac{f_l \, (f_r t_x - X_r t_z)}{X_r \, (r_{31} X_l + r_{32} Y_l + f_l r_{33}) - f_r \, (r_{11} X_l + r_{12} Y_l + f_l r_{13})} \end{cases} \tag{5}$$

Equation (5) is the expression of the three-dimensional reconstruction of the non-cooperative target.

C. A SYSTEM CONCEPT OF NON-COOPERATIVE TARGET CAPTURING BY USING DUAL-ARM SPACE ROBOT

As shown in Fig. 6, the process of on-orbit service to the non-cooperative target includes: launch phase, orbital transition phase, tracking and approaching, the contact collision, and the stable control of the compounded system after capturing, etc.

In view of the characteristics of the non-cooperative target, the dual-arm coordination method is used to capture the target, among them, a challenge work we need to solve is how to calculate the pose of the non-cooperative target, only in this way, and the arms can catch the target in the "coordinated" way. The main work in this article is that we proposed a new accuracy and efficiency pose measurement method for the non-cooperative target.

III. RELATIVE POSE MEASUREMENT FRAME AND ERROR ANALYSIS
A. ALGORITHM FLOWCHART

It's well known to all that stereo vision camera has sub-pixel accuracy limitation. The camera's unavoidable hardware error comes from the camera's mechanical structure and optical devices. To mitigate this limitation, we can improve the resolution and anti-interference ability of the camera. As a result, the manufacturing cost of the camera will become very high. In fact, the hardware error of an industrial camera is usually a pixel, which has little impact on our research. In order to reduce the overall error, we can use the effective calibration algorithm and visual measurement method to make up.

The algorithm flowchart of stereo vision-based pose measurement method is shown in Fig. 7. The whole pose
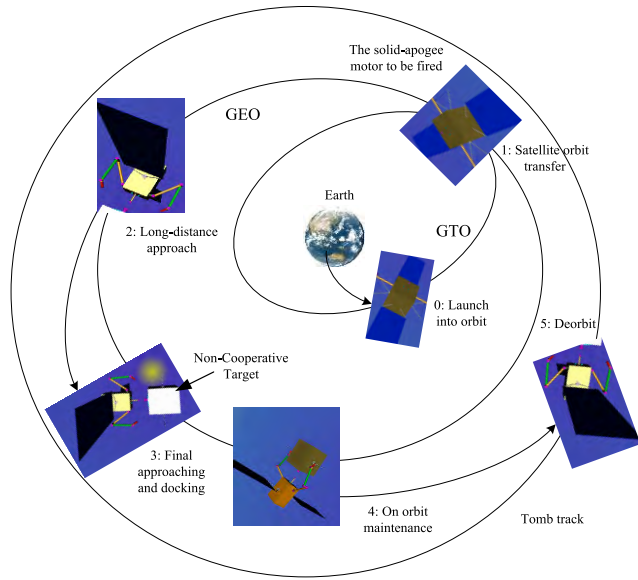
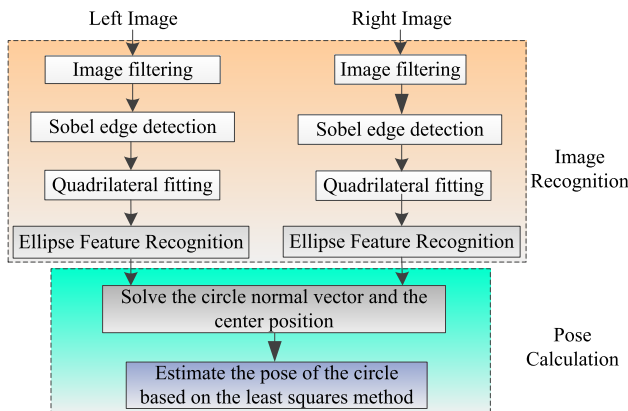**FIGURE 6.** The flow chart of dual-arm space robot in orbit service.

FIGURE 7. The algorithm flowchart of pose measurement based on stereo vision.

measurement process is mainly consisting of two parts: image recognition (i.e. image filtering, edge detection and ellipse recognition in 2D image plane) and pose calculation (normal vector and center position of the circular feature).

Because the key of this study is the final approaching and docking, the influence of the sun, earth and orbits on the visual measurement of the non-cooperative target is very small. In view of the complexity of the space environment, in the process of extracting ellipse, to eliminate some of the scattered noise caused by the peak of the spikes, the original image should be preprocessed by median filtering. Then the sobel operator is used to detect the elliptical contours of the space circle imaging. After that, we obtain the sub-pixel coordinates of the contour points by using the polynomial fitting method. Finally, the least square elliptic fitting method is used to fit these points into ellipses.

B. TRADITIONAL SOLVING METHOD AND ITS DISADVANTAGES

As shown in Fig. 8, E' is the imaging ellipse plane of the target circle plane E, the four endpoints of an ellipse on the imaging plane are b', c', p' and q', the corresponding four endpoints on the target plane are B, C, P and Q. The surface surrounded by red lines is called the largest viewing surface LAA(Largest Apex Angle).
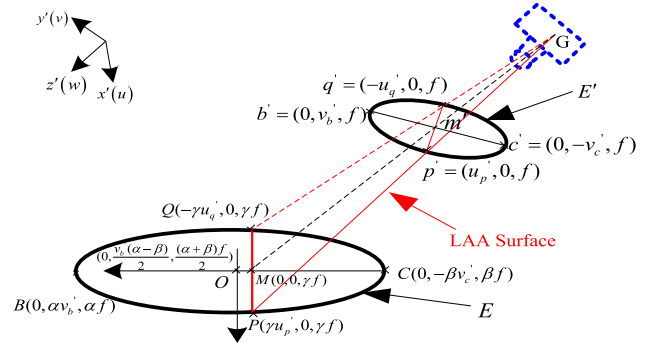

FIGURE 8. The schematic diagram of traditional monocular imaging.

According to Chen's [34] and Xu's [35] method of binocular measurement the pose of natural objects with circular or near-circular shape, when the optical axis of the camera coincides with the z'-axis, a new camera coordinate system is formed. Since the circle and the camera center are unchanged, then the largest observation surface of LAA is also unchanged.

Assuming that the radius of the circle is R_o, it is easy to get the position vector of the circular center according to the spatial geometry:

$$\begin{cases} \boldsymbol{O}_1 = \left(o_x, o_y, o_z\right)^{\mathrm{T}} \\ \quad = \left[0, \dfrac{R_o v_{b'}}{u_{p'}}\sqrt{\dfrac{u_{p'}^2 - v_{b'}^2}{v_{b'}^2 + f^2}}, \dfrac{R_o f}{u_{p'}}\sqrt{\dfrac{u_{p'}^2 + f^2}{v_{b'}^2 + f^2}}\right]^{\mathrm{T}} \\ \boldsymbol{O}_2 = \left(o_x, -o_y, o_z\right)^{\mathrm{T}} \end{cases} \quad (6)$$

The normal vector of the circle is:

$$\begin{cases} \boldsymbol{n}_1 = \left(n_x, n_y, n_z\right)^{\mathrm{T}} = \dfrac{\boldsymbol{PQ} \times \boldsymbol{BC}}{|\boldsymbol{PQ} \times \boldsymbol{BC}|} \\ \quad = \dfrac{\left[0, -f\sqrt{u_{p'}^2 - v_{b'}^2}, v_{b'}\sqrt{u_{p'}^2 + f^2}\right]^{\mathrm{T}}}{\sqrt{(u_{p'}^2 - v_{b'}^2)f^2 + (u_{p'}^2 + f^2)v_{b'}^2}} \\ \boldsymbol{n}_2 = \left(n_x, -n_y, n_z\right)^{\mathrm{T}} \end{cases} \quad (7)$$

From the expression of $\vec{n}$, we can see that the traditional analytic method in solving the attitude of the circular surface has nothing to do with radius, which can be directly obtained by the matching of normal vector.

From (6) and (7), let $k = l, r$, the position vector of the circle can be expressed as:

$$^{o_k}\boldsymbol{p}_{c_k} = [0, \pm A_k R_o, B_k R_o]^{\mathrm{T}} \quad (8)$$

where

$$A_k = \frac{v_{b'}}{u_{p'}}\sqrt{\frac{u_{p'}^2 - v_{b'}^2}{v_{b'}^2 + f^2}}, \quad B_k = \frac{f}{u_{p'}}\sqrt{\frac{u_{p'}^2 + f^2}{v_{b'}^2 + f^2}}.$$

According to binocular calibration results, the position vector of the circular surface unified into the left camera coordinate system can be expressed as:

$$\begin{cases} ^{or}\boldsymbol{p}_{cl} = {}^{cr}\boldsymbol{t}_{cl} + {}^{cr}\boldsymbol{R}_{cl}\boldsymbol{D}_r R_o^r \\ ^{ol}\boldsymbol{p}_{cl} = \boldsymbol{D}_l R_o^l \end{cases} \quad (9)$$

where $\boldsymbol{D}_k = [0, \pm A_k, B_k]^T$, R_o^l and R_o^r are the measurement radius of the left and right cameras, respectively.

Since $^{or}\boldsymbol{p}_{cl} = {}^{ol}\boldsymbol{p}_{cl}$, (9) can be simplified as:

$$\begin{bmatrix} \boldsymbol{D}_l - {}^{cr}\boldsymbol{R}_{cl}\boldsymbol{D}_r \end{bmatrix}\begin{bmatrix} R_o^l \\ R_o^r \end{bmatrix} = {}^{cr}\boldsymbol{t}_{cl} \quad (10)$$

For the solution of (10), the least squares method can be used, thus:

$$\begin{bmatrix} R_o^l \\ R_o^r \end{bmatrix} = \left(\boldsymbol{C}^T\boldsymbol{C}\right)^{-1}\boldsymbol{C}^T \cdot {}^{cr}\boldsymbol{t}_{cl} \quad (11)$$

where $\boldsymbol{C} = \begin{bmatrix} \boldsymbol{D}_l - {}^{cr}\boldsymbol{R}_{cl}\boldsymbol{D}_r \end{bmatrix}$.

Substituting (11) into (6) and (7), the radius and position vectors of the circular surface can be obtained by:

$$R_o = \frac{R_o^l + R_o^r}{2} \quad (12)$$

$$O_o = \frac{O_o^l + O_o^r}{2} \quad (13)$$

For traditional analytical method, substituting (11) into (6), we can get the pose of natural objects with circular shape. Xu [35] proposed a closed-form analytical method to estimate the pose of the circle's center, shown as Fig. 9. The method decomposed the pose measurement problem into two parts: the surface normal of the circular shape; based on the estimated normal vector, the center position vector of the circle is then calculated.
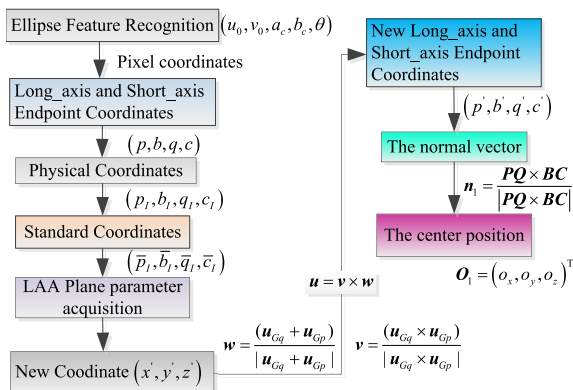

FIGURE 9. The detailed process of traditional solving method.

From the above derivation, it can be seen that the traditional method is complex in the conversion process of the new and

old coordinate system, and it is also the most time-consuming part of the whole algorithm. The ellipse is obtained by fitting the ellipse with the least squares method. These parameters themselves have some errors. The four vertices of the ellipse are further found from the five parameters, which can complete description of the ellipse. Then the pose solution is obtained according to the four vertices. In the calculation process, the error will be further amplified. In order to do quantitative analyses of the calculation time, here, we take 100 sets of elliptical parameters to do pose calculation experiment. The average computation time is 0.042s. According to the statistics, the new and old coordinate transformation process costs 43.98% of the total time. There is a big room for improvement.

C. SOLVING CONCEPT WITH HIGH ACCURACY

The traditional method is not efficient: 1) the coordinate system conversion process takes too long; 2) and the five parameters describing the ellipse are described as four vertex coordinates; 3) the process error occurs. To improve the accuracy and speed up the pose calculation process, a new efficient solving concept is presented. As shown in Fig. 10, it can be simplified as four steps: firstly, convert the ellipse pixel plane to the camera coordinate system through $\boldsymbol{A}$ matrix; secondly, convert the abovementioned system to the standard cut plane through $\boldsymbol{P}$ matrix; thirdly, convert the above cut plane to the standard circular cross-sections through $\boldsymbol{Q}$ matrix; finally, we can get the pose of the circular shape through the norm vector and eigenvalue.
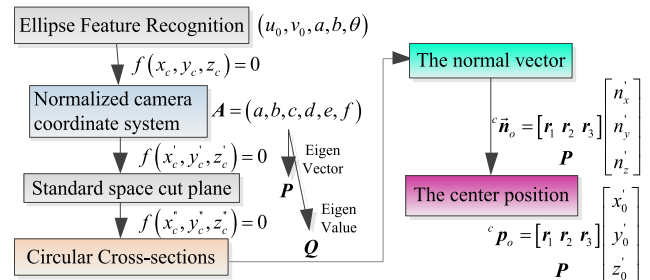

FIGURE 10. The detailed process of the new solving method.

The advantage of the new efficient method is that it directly uses the five independent parameters of the ellipse to do a complete spatial conic coordinate transformation, which reduces the process error. Moreover, the number of matrix conversions is reduced. The main conversion is solving $\boldsymbol{A}$ matrix, and the eigenvalues and eigenvectors of $\boldsymbol{A}$ matrix are mainly used in $\boldsymbol{Q}$ matrix and $\boldsymbol{P}$ Matrix, respectively. In addition, since the most time-consuming process of the whole pose measurement is actually an elliptical feature extraction, to speed up the image pre-processing and image recognition process, an FPGA-based parallel processing algorithm is proposed. The detail calculation process will describe in the next chapter.

IV. EFFICIENT SOLVING METHOD

A. IDEA OF STEREO VISION COLLABORATIVE MEASUREMENT

In terms of the pose measurement for space on-cooperative target mainly includes binocular vision, multi-vision and structural-light combination form. In view of the complexity of the space environment and the movement characteristics of the measurement target, binocular stereo vision is simple and reliable, low cost as well as flexible applications, etc. It is widely used in space measurement, industrial production and other fields. Conventional visual measurement needs to calculate the depth information by matching the adjacent frames. As long as the analytical operation of the space target can be obtained, the pose information can be then solved, which overcomes the shortcomings of the traditional method. Fig. 11 shows the three-dimensional visual measurement method for the space non-cooperative target. The relative relationship between the reference frame to left-camera coordinate system is $^{o_{cl}}T_{ref}$; the relative relationship between the two camera frame is $^{cr}T_{cl}$; and the relative relationship between the reference frame to right-camera coordinate system $^{o_{cr}}T_{ref}$. Therefore, the pose measurement problem can be equivalent to find the coupling relationship between the target ellipse in the left and right camera coordinate system.
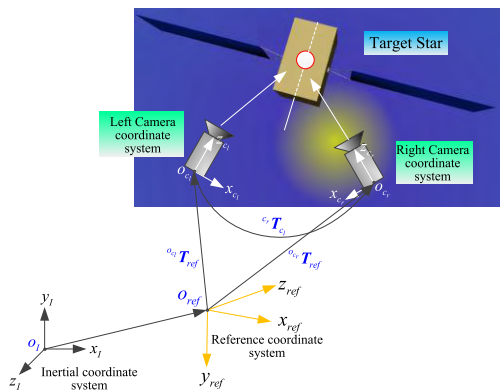
FIGURE 11. The diagrammatic sketch of stereo vision measurement.

Due to a lack of cooperative information on the space non-cooperative satellite, the identification of non-cooperative targets needs to be identified by their own inherent characteristics. According to the statistics of the launched spacecraft, it is clear that most of the emitters are rounded and the outer contours are almost quadrilateral. At the same time, because the circular cross section is easy to identify, the features that are not easily recognizable are prone to distortion and loss of information. Therefore, this paper uses the spacecraft body shape and the satellite surface cylinder as the recognition feature, and multi-feature recognition method is carried out by image processing. Thus, we can obtain the relative pose information of the non-cooperation target. Traditional identification methods are based on a single feature such as a rectangle or an ellipse as an identification target. Considering the influence of light and background noise, the linear feature

recognition algorithm has higher accuracy and robustness than the contour recognition algorithm, as shown in Fig. 12. In order to improve the robustness of the algorithm, this paper combines the ontology shape and circular features of the target in view of the complex motion characteristics of the space non-cooperative target. Even if part of the satellite is clipping, the system still able to get a stable pose measurement result, which improves the robustness of the algorithm.
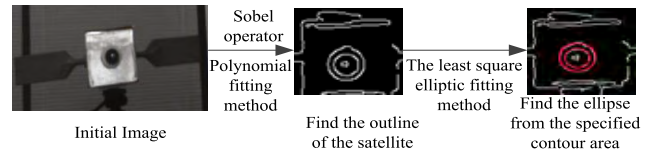
FIGURE 12. The schematic diagram of multi - feature identification.

B. PARALLEL COMPUTING FOR IMAGE PRE-PROCESSING OF POSE MEASUREMENT

As shown in Fig. 13, the idea of parallel computing for median filter is through a 3×3 sliding window to obtain the neighborhood of 9 pixel values. The window of each pixel is in descending order, and then the minimum, the middle and the maximum value of each column are used. Finally, we take $\{Min, Med, Max\}$ to do a sort, and take their median as the median of the window. The results of median filtering are shown in Fig. 14.
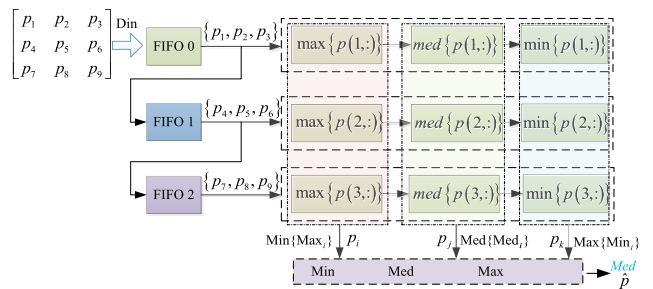
FIGURE 13. The parallel computing flow chart of Median filter.

The parallel computing idea of the sobel edge detection is to calculate the sum of each pixel convolution, and obtain the gradient value $\{G_X, G_Y\}$, and then obtain its square root through the Cordic IP core. According to the external input threshold δ, it is possible to determine whether the pixel (x, y) is the edge of the pixel or not. The entire parallel design flow is shown in Fig. 15, and the results of edge detection are shown in Fig. 16.

According to the edge detection results, we can get the pixel coordinates of the feature point (u, v). Assuming that the coefficient matrix of the elliptic equation is $N = [a\,b\,c\,d\,e\,f]$, and noting $X = [u^2, uv, v^2, u, v, 1]^T$, the elliptic equation can be rewritten as

$$f(u, v) = N \cdot X \qquad (14)$$

(a)

(b)

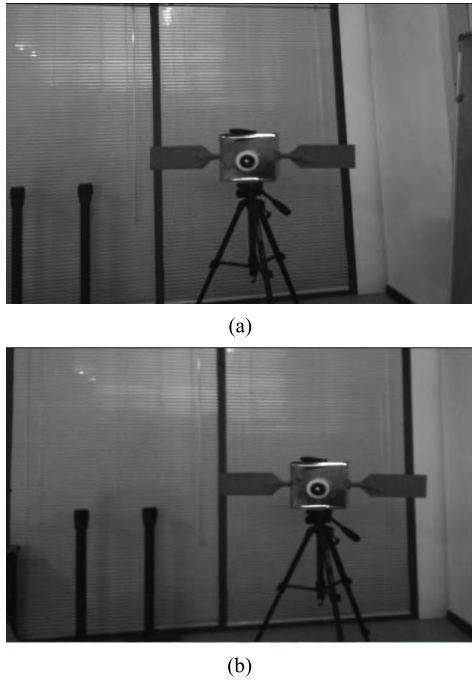**FIGURE 14.** The results of median filter base on FPGA. (a) The median filter of left camera. (b) The median filter of right camera.

(a)

(b)

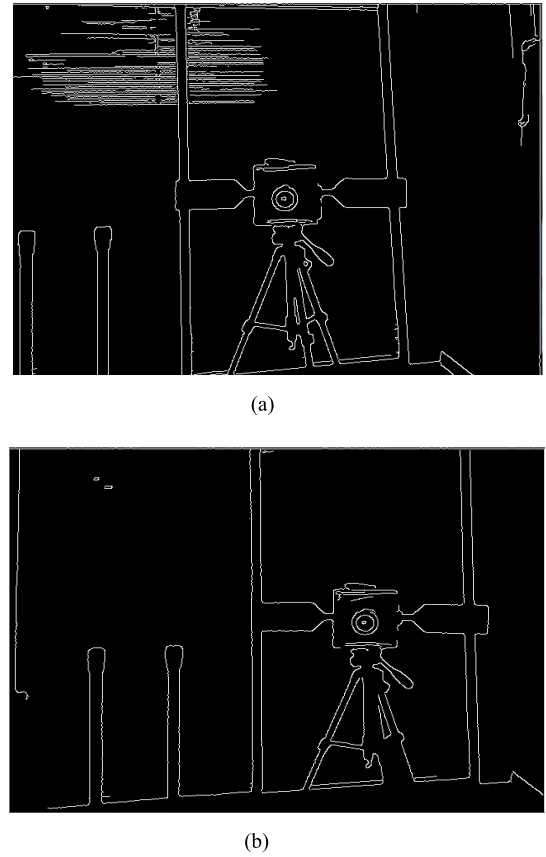**FIGURE 16.** The results of sobel edge detection based on FPGA. (a) The edge detection of left camera. (b) The edge detection of right camera.

TABLE 1. FPGA and PC comparisons.

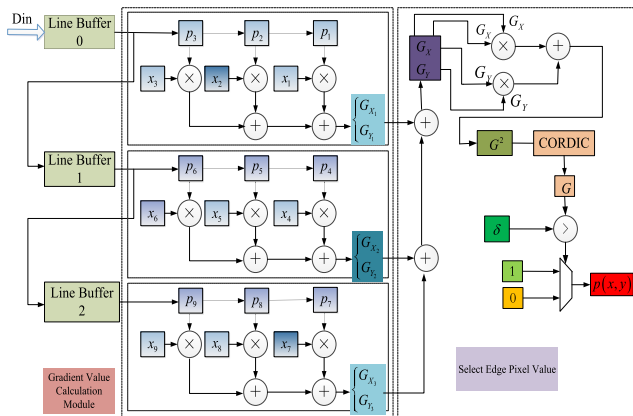| Classification	CPU	Image Size	Clock frequency	Average time
PC	i3-4170	2*640*480	3.7GHz	0.7397s
FPGA	Cyclone III	2*640*480	20 MHz	0.0222s

FIGURE 15. The parallel computation flowchart of sobel edge detection algorithm.

The problem of ellipse fitting is actually the minimum distance from all points to elliptic equations, so the problem of ellipse extraction can be degenerated to solve the optimal value of the objective function:

$$
\begin{aligned}
F\,(a, b, c, d, e, f) \\
= \min\left(\sum_{i=1}^{n} f^2\,(u_i, v_i)\right) = \min\left(\sum_{i=1}^{n} (N_i X_i)^2\right) \\
= \min\left(\sum_{i=1}^{n} N_i X_i X_i^T N_i^T\right)
\end{aligned} \tag{15}
$$

The measurement area extracted by satellite ontology and ellipse feature is shown in Fig. 17.

The MT series CMOS used in this paper has a frame rate of 60 fps at VGA resolution. FPGA's chip model is Cyclone III. The frequency of the chip clock is 20 MHz, and the frame rate of the image pre-processing is 45 fps. Compared to VC Studio 2010 software, the computer CPU is i3-4170, and the clock frequency is 3.7GHz, and the single frame average costs 0.739733s with the same image pre-processing. As shown in the TABLE 1, in case that the clock frequency is much slower than the PC host, the parallel processing speed of FPGA-based is 33 times faster than the host computer.

C. THE POSE SOLUTION FOR SPACE CIRCULAR FEATURE

The projection of the spatial circle is shown in Fig. 18, among them, $O_w - X_w Y_w Z_w$ is the world coordinate system; $O_c - X_c Y_c Z_c$ is the optical center of camera coordinate system; and $O_I - X_I Y_I$ is the image coordinate system.
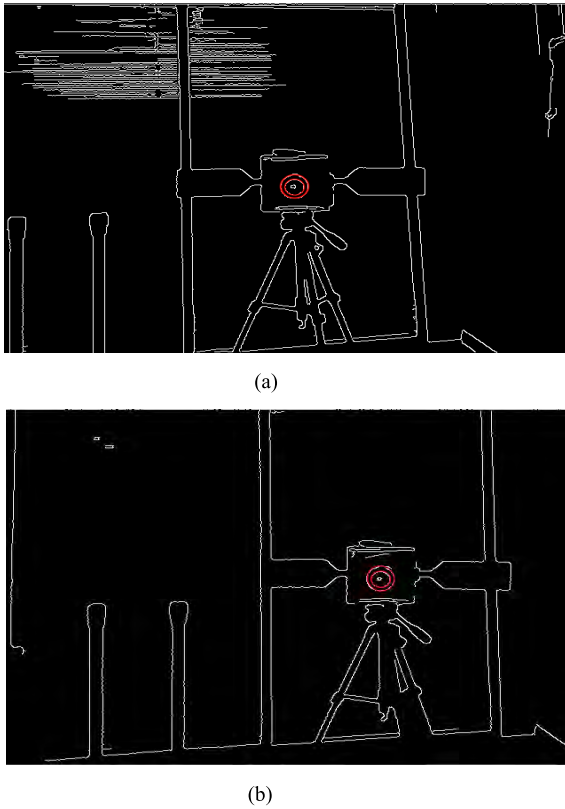
FIGURE 17. Ellipse feature extraction results of target surface. (a) The sketch map of extracting ellipse feature from left camera. (b) The sketch map of extracting ellipse feature from right camera.
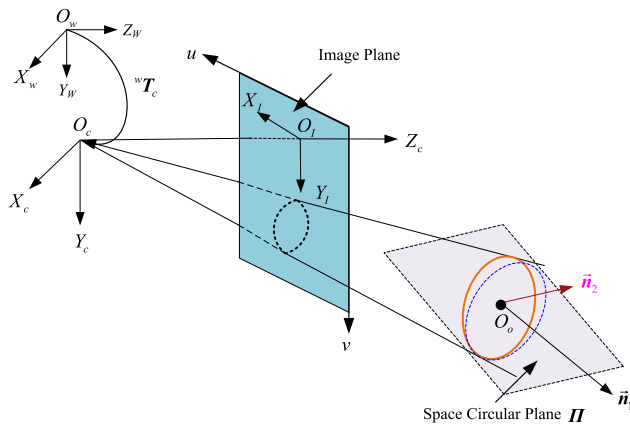

FIGURE 18. The projection schematic diagram of space circular feature.

The transformation matrix from the camera coordinate system to the world coordinate system is ${}^{w}T_{c}$; the measured space circle is on the plane Π; the center of the circle is O_{o} and the normal vector is $\vec{n}$.

The projection of the space circular shape on the image plane is an ellipse, and the optical center of the camera O, the ellipse image I and the spatial plane Π constitute the elliptical cone. The five parameters of the ellipse can be obtained by the feature extraction of the ellipse, that is, the center point (x_c, y_c), long and short axis (a_c, b_c) and rotation angle θ of

the a_c-axis relative to the $+x$-axis, thus the elliptical quadratic form can be further expressed as:

$$\left(\frac{(u - x_c)\cos\theta + (v - y_c)\sin\theta}{a_c}\right)^2$$
$$+ \left(\frac{-(u - x_c)\sin\theta + (v - y_c)\cos\theta}{b_c}\right)^2 = 1 \quad (16)$$

For the convenience of calculation, the elliptical plane is normalized, i.e.

$$\begin{bmatrix} u \\ v \\ 1 \end{bmatrix} = \begin{bmatrix} f_u & u_0 & 0 \\ 0 & f_v & v_0 \\ 0 & 0 & 1 \end{bmatrix} \begin{bmatrix} x_I \\ y_I \\ 1 \end{bmatrix}$$
$$= \frac{1}{z_c} \begin{bmatrix} f_u & u_0 & 0 \\ 0 & f_v & v_0 \\ 0 & 0 & 1 \end{bmatrix} \begin{bmatrix} x_c \\ y_c \\ z_c \end{bmatrix} \quad (17)$$

Substituting (17) into (16), the equation of the ellipse normalized focal plane can be rewritten as:

$$f(x_c, y_c, z_c) = ax_c^2 + by_c^2 + cx_c y_c + dx_c z_c + ey_c z_c + fz_c^2 = 0 \quad (18)$$

Among them, the coefficients of the elliptical quadratic form are as follow:

$$a = b_c^2 f_u^2 \cos^2\theta + a_c^2 f_u^2 \sin^2\theta \quad (19)$$

$$b = 2\left(b_c^2 - a_c^2\right) f_u f_v \cdot \sin\theta\cos\theta \quad (20)$$

$$c = a_c^2 f_v^2 \cos^2\theta + b_c^2 f_v^2 \sin^2\theta \quad (21)$$

$$d = -2\left(b_c^2\cos^2\theta + a^2\sin^2\theta\right) f_u \cdot x_c$$
$$- 2\left(b_c^2 - a_c^2\right)\sin\theta\cos\theta \cdot y_c$$
$$+ 2b_c^2\left(u_0\cos\theta + v_0\sin\theta\right) f_u\cos\theta$$
$$- 2a_c^2\left(-u_0\sin\theta + v_0\cos\theta\right) f_u\sin\theta \quad (22)$$

$$e = -2\left(b_c^2 - a_c^2\right) f_v\sin\theta\cos\theta \cdot x_c$$
$$- 2\left(a_c^2\cos^2\theta + b_c^2\sin^2\theta\right) f_v \cdot y_c$$
$$+ 2b_c^2\left(u_0\cos\theta + v_0\sin\theta\right) f_v\sin\theta$$
$$- 2a_c^2\left(-u_0\sin\theta + v_0\cos\theta\right) f_v\cos\theta \quad (23)$$

$$f = -\left(b_c^2\cos^2\theta + a_c^2\sin^2\theta\right) x_c^2$$
$$+ \left(a_c^2\cos^2\theta - b_c^2\sin^2\theta\right) y_c^2$$
$$- 2\left(b_c^2 + a_c^2\right)\sin\theta\cos\theta \cdot x_c y_c$$
$$+ \left[-2b_c^2\left(u_0\cos\theta + v_0\sin\theta\right)\cos\theta\right.$$
$$\left. + 2a_c^2\left(-u_0\sin\theta + v_0\cos\theta\right)\sin\theta\right] x_c$$
$$+ \left[-2b_c^2\left(u_0\cos\theta + v_0\sin\theta\right)\sin\theta\right.$$
$$\left. - 2a_c^2\left(-u_0\sin\theta + v_0\cos\theta\right)\cos\theta\right] y_c$$
$$+ \left[b_c^2\left(u_0\cos\theta + v_0\sin\theta\right)^2\right.$$
$$\left. + a_c^2\left(-u_0\sin\theta + v_0\cos\theta\right)^2 - a_c^2 b_c^2\right] \quad (24)$$

The oblique conic equation (18) can be rewritten as:

$$f(x_c, y_c, z_c) = X_c^{\mathrm{T}} \cdot A \cdot X_c = 0 \qquad (25)$$

where

$$A = \begin{bmatrix} a & c/2 & d/2 \\ c/2 & b & e/2 \\ d/2 & e/2 & f \end{bmatrix}, \quad X_c = [x_c, y_c, z_c]^{\mathrm{T}}.$$

According to the matrix theory, the real symmetric matrix A can be transformed into a standard form $diag(A)$ by line transformation and column transformation, that is, the oblique cone can be converted into a standard cone through coordinate transformation.

For the 3$^{\text{th}}$ real symmetric matrix A, there is an orthogonal matrix P makes $P^{-1}AP$ to a diagonal matrix, that is,

$$P^{-1}AP = P^{\mathrm{T}}AP = \begin{bmatrix} \lambda_1 & & \\ & \lambda_2 & \\ & & \lambda_3 \end{bmatrix} \qquad (26)$$

Assuming that $X_c = P \cdot [x'_c, y'_c, z'_c]^{\mathrm{T}}$, let x'_c, y'_c, z'_c be the standard spatial coordinate system, then the quadratic type of space oblique cone can be rewritten as a standard formula:

$$\lambda_1 x_c'^2 + \lambda_2 y_c'^2 + \lambda_3 z_c'^2 = 0 \qquad (27)$$

According to the definition of the standard cone, in (27) there must be two symbols identical and opposite to the third, there is a special case here, when the projection of the space circle on the image plane is a circle, the oblique cone can be degenerated into a positive cone, in this case, the two eigenvalues of the same sign are equal.

From the matrix theory, assuming that the eigenvalues of matrix A are $\lambda_1(A), \lambda_2(A), \lambda_3(A)$, the corresponding normalized eigenvectors are $\vec{n}_1(A), \vec{n}_2(A), \vec{n}_3(A)$, then we get

$$(\lambda I - A)x = 0 \qquad (28)$$

Where, $I \in R^{3\times3}$ is a unit matrix, λ is the eigenvalues of A and x is the eigenvector of A.

Write P as a column vector form $[\vec{r}_1 \ \vec{r}_2 \ \vec{r}_3]$, without loss of generality, let $\lambda_1(A) \geq \lambda_2(A) > 0$, there is

$$\begin{cases} \lambda_1 = \lambda_1(A) \\ \lambda_2 = \lambda_2(A) \\ \lambda_3 = \lambda_3(A) \end{cases} \qquad (29)$$

$$\begin{cases} \vec{r}_3 = (-1)^{1+sgn(\vec{n}_3(A)_z)} \vec{n}_3(A) \\ \vec{r}_2 = \vec{n}_2(A) \\ \vec{r}_1 = \vec{r}_2 \times \vec{r}_3 \end{cases} \qquad (30)$$

where $sgn(x) = \begin{cases} 1, & x > 0 \\ 0, & x < 0. \end{cases}$

As shown in Fig. 18, the elliptical cone intersects the circle to form a truncated surface, and its normal vector is expressed as (n'_x, n'_y, n'_z), the expression of the circle in the standard space coordinate system is

$$n'_x x'_c + n'_y y'_c + n'_z z'_c = h_0 \qquad (31)$$

where $n_x'^2 + n_y'^2 + n_z'^2 = 1$.

(a) When $n_x'^2 + n_y'^2 \neq 0$, in order to facilitate the subsequent calculation [27], the z''_c-axis coincides with the normal vector (n'_x, n'_y, n'_z) of the cut-off surface by attitude transformation, the transformation relationship is:

$$X'_c = QX''_c = [\vec{r}'_1, \vec{r}'_2, \vec{r}'_3] X''_c \qquad (32)$$

where

$$\vec{r}'_3 = [n'_x, n'_y, n'_z]^{\mathrm{T}},$$

$$\vec{r}'_2 = \left[\frac{-n'_x n'_z}{\sqrt{n_x'^2 + n_y'^2}}, \frac{-n'_y n'_z}{\sqrt{n_x'^2 + n_y'^2}}, 0 \right]^{\mathrm{T}},$$

$$\vec{r}'_1 = \left[\frac{-n'_y}{\sqrt{n_x'^2 + n_y'^2}}, \frac{n'_x}{\sqrt{n_x'^2 + n_y'^2}}, 0 \right]^{\mathrm{T}}.$$

Substituting (32) into (31) yields the circle plane equation:

$$z''_c = h_0 \qquad (33)$$

Simultaneous equations (33) and (32), we can obtain the line of intersection equation of the circle:

$$f(x''_c, y''_c, z''_c) = X_c''^{\mathrm{T}} \cdot \hat{A} \cdot X''_c = 0 \qquad (34)$$

where

$$\hat{A} = \begin{bmatrix} \hat{a} & \hat{c}/2 & \hat{d}/2 \\ \hat{c}/2 & \hat{b} & \hat{e}/2 \\ \hat{d}/2 & \hat{e}/2 & \hat{f} \end{bmatrix}, \quad X''_c = [x''_c, y''_c, z''_c]^{\mathrm{T}}.$$

For the quadratic equation (34), in order to make it a circle, the following conditions need to be satisfied:

$$\begin{cases} \hat{b} = \dfrac{2n'_x n'_y n'_z (\lambda_1 - \lambda_2)}{n_x'^2 + n_y'^2} = 0 \\ \hat{a} = \dfrac{\lambda_1 n_y'^2 + \lambda_2 n_x'^2}{n_x'^2 + n_y'^2} = \hat{c} \\ \quad = \dfrac{\lambda_1 n_x'^2 n_z'^2 + \lambda_2 n_y'^2 n_z'^2}{n_x'^2 + n_y'^2} + \lambda_3 (n_x'^2 + n_y'^2) \end{cases} \qquad (35)$$

For the solution of the equation(35), the analysis is as follows:

a) If $n'_x = 0 \cap n'_z = 0$, then, there is no solution;

b) If $n'_y = 0$, we can get:

$$^c\vec{n}'_o = \begin{bmatrix} n'_x \\ n'_y \\ n'_z \end{bmatrix} = \begin{bmatrix} \pm\sqrt{\dfrac{\lambda_1 - \lambda_2}{\lambda_1 - \lambda_3}} \\ 0 \\ -\sqrt{\dfrac{\lambda_2 - \lambda_3}{\lambda_1 - \lambda_3}} \end{bmatrix} \qquad (36)$$

Assuming that the radius of the circle is R_o, substituting (36) into (34) yields

$$x_c''^2 + \left[y''_c - \frac{h_0 n'_x n'_z}{\lambda_2} (\lambda_1 - \lambda_3) \right]^2 = R_o^2 \qquad (37)$$

where

$$R_o = \sqrt{\left(\frac{\lambda_1 - \lambda_3}{\lambda_2}h_0 n'_x n'_z\right)^2 - \frac{h_0^2}{\lambda_2}\left(\lambda_1 n'^2_x + \lambda_3 n'^2_z\right)}.$$

Simultaneous (34), (33) and (30), the center of the circle expressed in the coordinate system $o''_c - x''_c y''_c z''_c$ is

$$^c\boldsymbol{p}''_o = \begin{bmatrix} x''_0 \\ y''_0 \\ z''_0 \end{bmatrix} = \begin{bmatrix} 0 \\ \pm\sqrt{-\frac{(\lambda_1 - \lambda_2)(\lambda_2 - \lambda_3)}{\lambda_1 \lambda_3}} R_o \\ \frac{\lambda_2}{\sqrt{-\lambda_1 \lambda_3}} R_o \end{bmatrix} \quad (38)$$

Substituting (38) into (32) gives the representation of the center coordinates in the standard space $o'_c - x'_c y'_c z'_c$ is:

$$^c\boldsymbol{p}'_o = \begin{bmatrix} x'_0 \\ y'_0 \\ z'_0 \end{bmatrix} = \begin{bmatrix} \pm\sqrt{-\frac{\lambda_3(\lambda_1 - \lambda_2)}{\lambda_1(\lambda_1 - \lambda_3)}} R_o \\ 0 \\ \sqrt{-\frac{\lambda_1(\lambda_2 - \lambda_3)}{\lambda_3(\lambda_1 - \lambda_3)}} R_o \end{bmatrix} \quad (39)$$

Equation (39) and (36) are multiplied by the orthogonal transformation matrix $\boldsymbol{P}$, respectively. The pose of the circle in the camera coordinate system can be expressed as:

$$^c\boldsymbol{p}_o = \begin{bmatrix} ^c x_o \\ ^c y_o \\ ^c z_o \end{bmatrix} = \boldsymbol{P} \begin{bmatrix} x'_0 \\ y'_0 \\ z'_0 \end{bmatrix} = \begin{bmatrix} \vec{r}_1 & \vec{r}_2 & \vec{r}_3 \end{bmatrix} \begin{bmatrix} x'_0 \\ y'_0 \\ z'_0 \end{bmatrix} \quad (40)$$

$$^c\vec{\boldsymbol{n}}_o = \begin{bmatrix} ^c n_x \\ ^c n_y \\ ^c n_z \end{bmatrix} = \boldsymbol{P} \begin{bmatrix} n'_x \\ n'_y \\ n'_z \end{bmatrix} = \begin{bmatrix} \vec{r}_1 & \vec{r}_2 & \vec{r}_3 \end{bmatrix} \begin{bmatrix} n'_x \\ n'_y \\ n'_z \end{bmatrix} \quad (41)$$

(b) When $n'^2_x + n'^2_y = 0$, then

$$^c\vec{\boldsymbol{n}}'_o = \begin{bmatrix} n'_x \\ n'_y \\ n'_z \end{bmatrix} = \begin{bmatrix} 0 \\ 0 \\ 1 \end{bmatrix} \quad (42)$$

Substituting (42) into (31) yields:

$$z'_c = h_0 \quad (43)$$

Simultaneous (43) and (27), the center position of the circle in the standard space $o'_c - x'_c y'_c z'_c$ are expressed as:

$$^c\boldsymbol{p}'_o = \begin{bmatrix} x'_0 \\ y'_0 \\ z'_0 \end{bmatrix} = \begin{bmatrix} 0 \\ 0 \\ \pm\sqrt{-\frac{\lambda_1}{\lambda_3}} R_o \end{bmatrix} \quad (44)$$

Similarly, (44) and (42) are multiplied by the orthogonal transformation matrix $\boldsymbol{P}$, respectively. We can obtain the pose of the circle in the camera coordinate system:

$$^c\boldsymbol{p}_o = \begin{bmatrix} ^c x_o \\ ^c y_o \\ ^c z_o \end{bmatrix} = \boldsymbol{P} \begin{bmatrix} x'_0 \\ y'_0 \\ z'_0 \end{bmatrix} = z'_0 \boldsymbol{r}_3 \quad (45)$$

$$^c\vec{\boldsymbol{n}}_o = \begin{bmatrix} ^c n_x \\ ^c n_y \\ ^c n_z \end{bmatrix} = \boldsymbol{P} \begin{bmatrix} n'_x \\ n'_y \\ n'_z \end{bmatrix} = \boldsymbol{r}_3 \quad (46)$$

From the calculation process of the pose of the circle, it can be seen that if we know the radius of the circle, we can obtain its pose by the new efficient method mentioned in the text. But for the space non-cooperative target, the geometry of the grasp handle is unknown; the number of equations is less than the number of unknowns, therefore, based on the above analysis method cannot directly find the pose information of the capture surface, which requires binocular collaborative measurement to obtain the pose information.

D. STEREO-VISION COLLABORATIVE MEASUREMENT

As shown in Fig. 19, among them, $O_w - X_w Y_w Z_w$ is the world coordinate system, $O_{c_l} - X_{c_l} Y_{c_l} Z_{c_l}$ is the left-arm hand-eye camera optical coordinate system, the left camera coordinate system relative to the world coordinate system transformation matrix is $^{c_l}\boldsymbol{T}_w$, $O_{c_r} - X_{c_r} Y_{c_r} Z_{c_r}$ is the right-arm hand-eye camera optical coordinate system, the right camera coordinate system relative to the right camera coordinate system transformation matrix is $^{c_r}\boldsymbol{T}_{c_l}$, $O_{I_l} - X_{I_l} Y_{I_l}$, $O_{I_r} - X_{I_r} Y_{I_r}$ are the left and right camera image coordinate system, respectively. The measured circle plane is $\Re$, the corresponding position vector of the center circle is O^l_o and O^r_o, respectively, and the normal vector is $\vec{n}^l_{circle}$ and $\vec{n}^r_{circle}$, respectively.
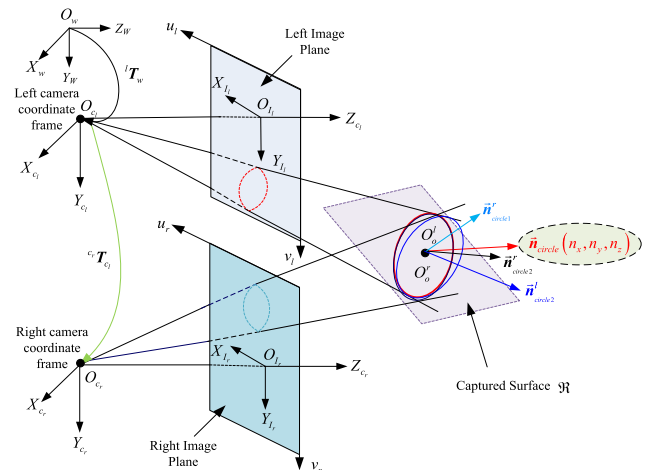
FIGURE 19. The schematic diagram of stereo vision measurement.

Similarly, seen from the expression of $^c\vec{\boldsymbol{n}}_o$, we know that the attitude calculation of the circular shape with the new efficient method has nothing to do with the radius, thus, we can use the similar method to solve it.

According to binocular calibration results, the pose of circular measured by the right camera can be expressed in the left camera coordinate system:

$$^{o_r}\boldsymbol{p}_{c_l} = {}^{c_r}\boldsymbol{t}_{c_l} + {}^{c_r}\boldsymbol{R}_{c_l} {}^{o_r}\boldsymbol{p}_{c_r} \quad (47)$$

$$^{o_r}\boldsymbol{R}_{c_l} = {}^{c_r}\boldsymbol{R}_{c_l} {}^{o_r}\boldsymbol{R}_{c_r} \quad (48)$$

Since $^{o_r}\boldsymbol{p}_{c_i} = \boldsymbol{P}\boldsymbol{A}_i (i = l, r)$, (47) can be further simplified as:

$$[\boldsymbol{P}\boldsymbol{A}_l - {}^{c_r}\boldsymbol{R}_{c_l}\boldsymbol{P}\boldsymbol{A}_r] \begin{bmatrix} R^l_o \\ R^r_o \end{bmatrix} = {}^{c_r}\boldsymbol{t}_{c_l} \quad (49)$$

efficient method introduces the coefficient matrix A of the elliptic equation, which reduce the computational complexity and improve the accuracy, the experiment will be mentioned later.

V. EXPERIMENTS

A. EXPERIMENTAL PLATFORM

Aiming at the stereo-vision measurement method mentioned in this paper, the validity of the whole measurement algorithm is verified by experiments, which can provide reliable pose information for the space robots coordinated capture the non-cooperative target. The whole experimental system mainly consists of three parts: FPGA-based binocular camera system, laser tracker and visual measurement software system. The composition diagram of the entire experimental system is shown in Fig. 21, which has three computing units: one is the FPGA-based acceleration processing unit, the main tasks of it is image pre-processing and image recognition; the second is the pose calculation unit, mainly responsible for attitude calculation; the last is the auxiliary measurement of the laser tracker, mainly calculate the three-dimensional coordinates of the target point as the reference value of the visual measurement by the built-in optical measurement software.
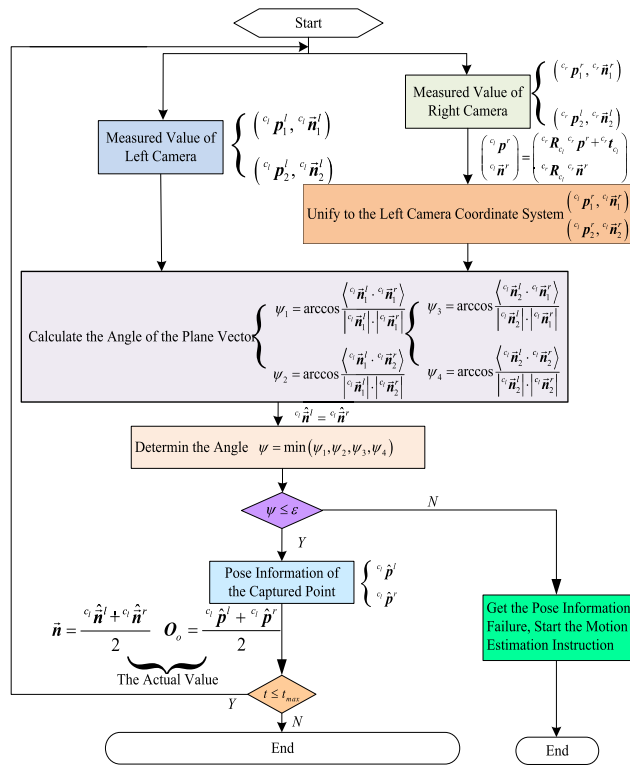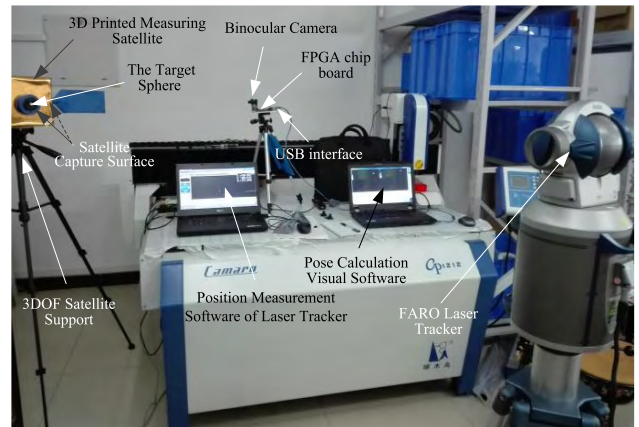

FIGURE 20. Computational flowchart of collaborative measurement the pose of the capture-point based on stereo vision.

where

$$
A_i = \begin{cases} \left[\pm\sqrt{\dfrac{\lambda_3(\lambda_1 - \lambda_2)}{\lambda_1(\lambda_1 - \lambda_3)}} \quad 0 \quad \sqrt{-\dfrac{\lambda_1(\lambda_2 - \lambda_3)}{\lambda_3(\lambda_1 - \lambda_3)}} \right]^T, \\ \hspace{3cm} \left(n'_y = 0\right) \\[4pt] \left[0 \quad 0 \quad \pm\sqrt{-\dfrac{\lambda_1}{\lambda_3}} \right]^T, \quad \left(n'^2_x + n'^2_y = 0\right). \end{cases}
$$

The least squares method can be used to solve (49), thus:

$$
\begin{bmatrix} R^l_o \\ R^r_o \end{bmatrix} = \left(B^T B\right)^{-1} B^T \left({}^{c_r}t_{c_l}\right) \tag{50}
$$

where $B = \begin{bmatrix} PA_l - {}^{c_r}R_{c_l}PA_r \end{bmatrix}$, R^l_o and R^r_o are the radius measured by the left and right cameras, respectively.

(a) If $n'^2_x + n'^2_y \neq 0$, substituting (50) into (40) and (41), we can get the pose of the target with circular shape;

(b) If $n'^2_x + n'^2_y = 0$, similarly, substituting (50) into (45) and (46), we can also obtain the pose of the target with circular shape.

According to the derivation of section IV-C, each measurement can get two sets of solutions, in order to obtain the normal vector of target surface, we can compare with the angle between the two normal vectors of the left camera and the right camera in the left camera coordinate system, the detailed process is shown in Fig. 20.

Compared the traditional method with the new efficient method, we can see that the expression form of the circular radius is very similar; the only difference is that the new

FIGURE 21. The schematic diagram of stereo-vision measurement system.

The binocular vision system chosen in this paper is a low cost Altera FPGA development board with two MT9T001 series CMOS cameras, the composition of the image acquisition system is shown in Fig. 22. The button can be used to switch the single/double output mode; taking into account the image pre-processing (median filtering, edge detection and ellipse detection) of the visual algorithm is time-consuming and resource consuming, and it is also very suitable for parallel computing, in this paper, the pre-processing algorithm of stereo vision measurement is written into the FPGA chip with Verilog language, the result(TABLE 1) shows that it can improve the calculation speed of the stereo vision system significantly.

Fig. 23 shows the three-dimensional structure of the measurement target by 3-D printing. The diameter of the capture cylinder is 80mm.
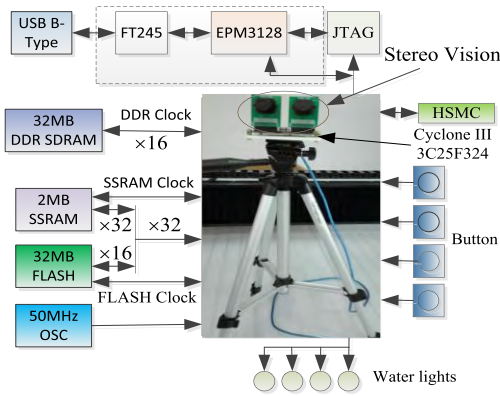
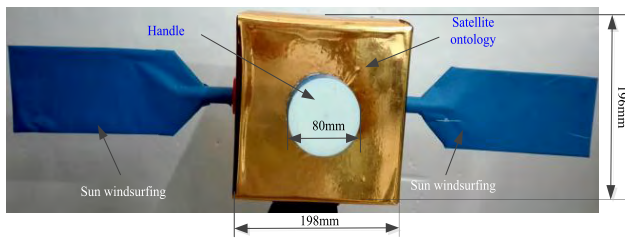**FIGURE 22.** The composition of the binocular vision acquisition system.

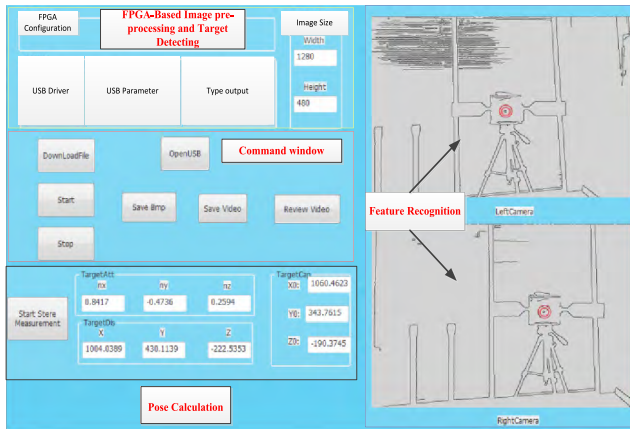**FIGURE 23.** Three-dimensional structure of 3D printing target satellite.

FIGURE 24. The block diagram of visual measurement software.

B. EXPERIMENTAL RESULTS AND ANALYSIS

In order to facilitate the visual operation, here, we set up MFC visual software based on FPGA + CPU architecture. The extraction of circular shape on the non-cooperative satellite is realized by FPGA, then, the extracted ellipse features are transmitted from FPGA to the CPU host computer through USB interface, and the subsequent pose calculation work is completed, among them, USB transmission mode is the Slave FIFOs' Role in the EZ-USB System. The whole block diagram of visual measurement software is shown in Fig. 24.

The visual measurement of the target in this paper mainly includes four aspects: image acquisition, target recognition, calibration (binocular calibration and external parameters calibration) and pose calculation:

(a) The main process of image acquisition is the initialization of CMOS register by FPGA;

(b) Visual recognition as a part of pre-processing for the visual measurement, mainly used to identify the capture surface by using the combination of quadrilateral and circular features of satellite surface, the sobel operator and the elliptic fitting method based on the least squares method are used to improve the robustness the process of target recognition;

(c) The binocular calibration and external parameter calibration is mainly used to determine the homogeneous transformation matrix between the camera frame and the reference coordinate system, its accuracy directly affects the accuracy of the pose measurement;

(d) The pose of natural objects with circular or near-circular shape is solved by new efficient method, compared with the traditional analytic method, the computational complexity is obviously reduced, and the measurement accuracy is obviously improved, which is beneficial for the real-time performance of the pose calculation system.

The overall pose measurement process is shown in Fig. 25. The FPGA processing part and the PC processing part are highlighted in detail.

1) EXTERNAL PARAMETERS CALIBRATION EXPERIMENTAL

The schematic diagram of external parameter calibration system is shown in Fig. 26, among them, $^{ref_j}T_{ref_i}$ is the homogeneous transformation matrix of the reference coordinate system from i state to j state; $^{c_j}T_{c_i}$ is the homogeneous transformation matrix of the camera coordinate system from i state to j state; $^{ref_i}T_{c_i}$ is the relative position and attitude transformation matrix between the camera coordinate system and the reference coordinate system; $^{ref}T_w$ is the homogeneous transformation matrix of the world coordinate system to the reference coordinate system and $^{c}T_b$ is the homogeneous transformation matrix of the base coordinate system to the camera coordinate system.

After coordinate transformation, $^{ref_j}T_{ref_i}$, $^{c_j}T_{c_i}$ and $^{ref_i}T_{c_i}$ meets the following relationship:

$$^{ref_j}T_{ref_i}{}^{ref_i}T_{c_i} = {}^{ref_j}T_{c_j}{}^{c_j}T_{c_i} = {}^{ref_i}T_{c_i}{}^{c_j}T_{c_i}$$

$$\Downarrow Format : AX = XB$$

$$\begin{bmatrix} ^{ref_j}R_{ref_i} & ^{ref_j}t_{ref_i} \\ O_{3\times1} & 1 \end{bmatrix} \begin{bmatrix} ^{ref_i}R_{c_i} & ^{ref_i}t_{c_i} \\ O_{3\times1} & 1 \end{bmatrix}$$
$$= \begin{bmatrix} ^{ref_i}R_{c_i} & ^{ref_i}t_{c_i} \\ O_{3\times1} & 1 \end{bmatrix} \begin{bmatrix} ^{c_j}R_{c_i} & ^{c_j}t_{c_i} \\ O_{3\times1} & 1 \end{bmatrix} \quad (51)$$

By expanding (51), the basic equation for external parameter calibration can be expressed as:

$$\begin{cases} ^{ref_j}R_{ref_i}{}^{ref_i}R_{c_i} = {}^{ref_i}R_{c_i}{}^{c_j}R_{c_i} \\ \left(^{ref_j}R_{ref_i} - I_{3\times3}\right)^{ref_i}t_{c_i} = {}^{ref_i}R_{c_i}{}^{c_j}t_{c_i} - {}^{ref_j}t_{ref_i} \end{cases} \quad (52)$$

It can be seen from (52) that the problem of external parameter calibration is actually the process of solving $^{ref_i}R_{c_i}$
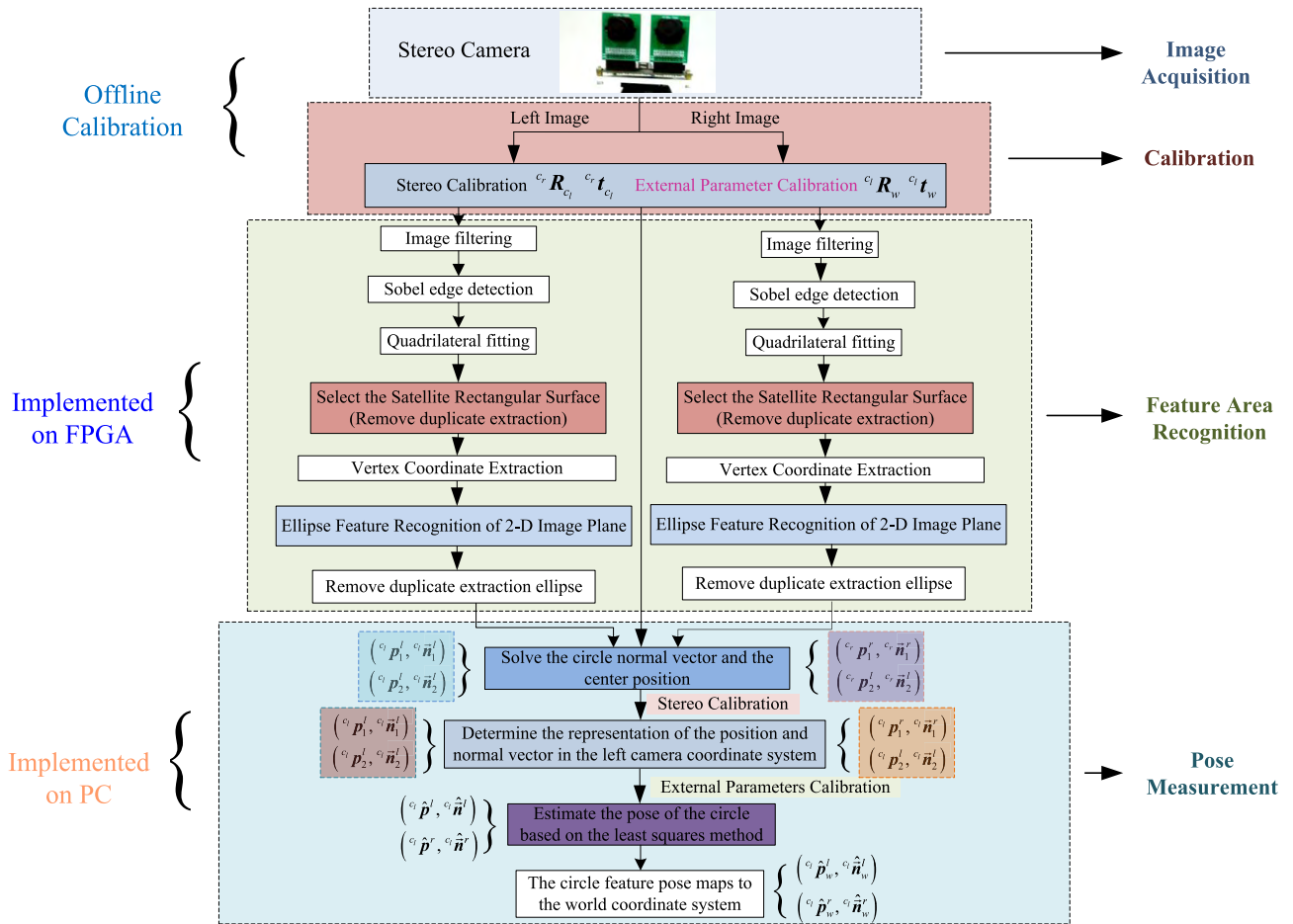
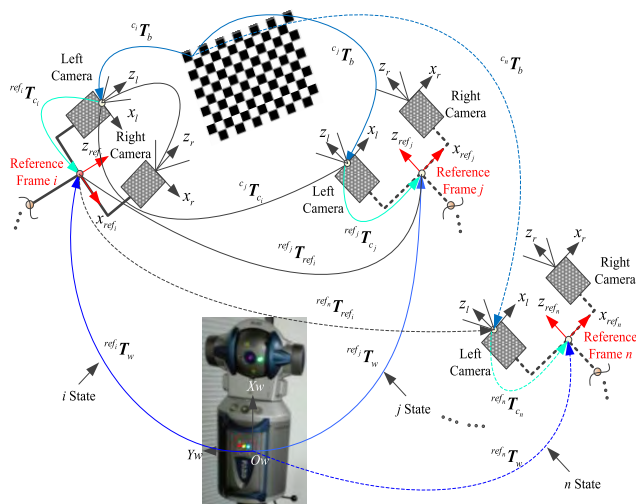**FIGURE 25.** The flow chart of pose measurement based on stereo vision.

FIGURE 26. The sketch map of external parameters calibration.

FIGURE 27. External parameters calibration for laser tracker and camera coordinate system.

In order to verify the effectiveness of the measurement method, the relationship between the camera coordinate system and the reference coordinate system at the end of the equivalent manipulator is calibrated with a high-precision PARO laser tracker.

The collaborative calibration diagram of the FARO laser tracker and the camera coordinate system is shown in Fig. 27.

and $^{ref_i}t_{c_i}$. The basic idea is to optimize the solution of $AX = XB$, many scholars have studied the methods of external parameter calibration (refer to [28]–[32]).
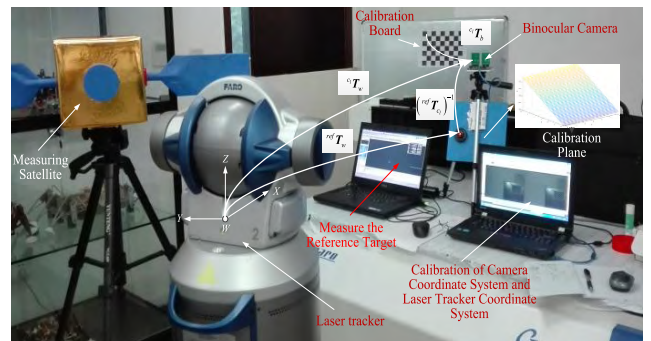
TABLE 2. The pose error analysis table of the capture point 1.

Name	Traditional analytic method of measurement error				The proposed new efficient method of measurement error			
	Position error /mm			normal vector deviation /°	Position error /mm			normal vector deviation /°
	x_{old}^1	y_{old}^1	z_{old}^1	θ_{old}^1	x_{new}^1	y_{new}^1	z_{new}^1	θ_{new}^1
1	4.0172	-4.8638	1.2784	2.1910	-1.9122	1.3653	-1.8193	1.8073
2	4.6690	2.2227	-0.7400	2.8291	2.0998	2.8583	1.1955	0.7353
3	4.2085	3.4534	1.5646	1.1971	-3.3170	-2.9721	2.1941	0.2906
4	4.3538	2.3244	8.9358	0.8564	3.6419	-1.2537	2.4914	0.8236
5	5.4308	4.5440	-4.9204	1.0108	1.7605	-2.2409	1.4363	0.2903
6	6.0634	8.3158	6.3481	0.5432	1.7333	1.2103	1.0181	1.5509
7	5.6245	6.2439	4.9235	3.0390	-1.3698	2.0758	-1.9375	1.7728
8	5.2925	6.5524	5.8109	2.2354	-2.8805	-2.1599	1.7125	0.6776
9	5.9512	4.5839	-6.2316	0.9037	1.7587	-1.8914	1.1927	0.8482
10	3.3969	4.6679	-4.7626	1.3371	-2.2281	-1.0579	-2.1097	1.7963
11	2.7605	4.9408	5.5850	0.9153	1.7729	-1.8716	-1.7932	0.7110
12	-7.6626	-4.9346	7.3701	0.4902	1.4463	3.1865	-3.2896	0.2646

According to above derivation, it is assumed that the checkerboard is not moved, and moves the binocular camera for multiple times($n = 20$), we can calculate the external calibration matrix of the reference coordinate system relative to the left-camera coordinate system, noted as $^{ref}T_{cl}$.

The homogeneous transformation matrix of the reference point relative to the laser tracker coordinate system is

$$^{ref}T_w = \begin{bmatrix} 0.4249 & -0.6758 & 0.6023 & 46.1251 \\ 0.5722 & -0.3151 & -0.7572 & 1828.6190 \\ 0.7015 & 0.6663 & 0.2528 & -345.1660 \\ 0 & 0 & 0 & 1 \end{bmatrix}$$
(53)

Therefore, the homogeneous transformation matrix of the left-camera coordinates system relative to the laser tracker coordinate system:

$$^{cl}T_w = \left(^{ref}T_{cl}\right)^{-1} \cdot {}^{ref}T_w$$

$$= \begin{bmatrix} 0.2892 & 0.9630 & 0.4681 & 1157.1 \\ 0.6216 & 0.3732 & -0.7131 & 1882.1 \\ -0.6613 & 0.8325 & -0.2556 & 1513.9 \\ 0 & 0 & 0 & 1 \end{bmatrix}$$
(54)

2) STEREO-VISION COLLABORATIVE MEASUREMENT EXPERIMENTAL

It should be noted that the later forms and pictures mentioned in the "the traditional methods" on behalf of the text mentioned in the third section of the traditional method. The theoretical analysis of the high precision and high efficiency measurement method proposed in this paper is shown in Section III-C.

Taking the first set of experiments as an example, according to the recognition result of the ellipse, we can get the ellipse parameters of the non-cooperative target

corresponding to the left and right cameras:

$$\begin{pmatrix} u_0 & v_0 & a & b & \theta \end{pmatrix}$$
$$= \begin{cases} E_L : (329\ 251\ 16\ 16\ -179.4555) \\ E_R : (424\ 229\ 15\ 17\ -13.3488) \end{cases}$$
(55)

The pose of natural objects with circular or near-circular shape obtained by the traditional method is:

$$\begin{cases} (\tilde{n}_{cir})_{old} = [0.8205, -0.4995, 0.2779]^T \\ \left(\tilde{O}_o\right)_{old} = [1008.1, 425.3, -221.3]\ (mm) \end{cases}$$
(56)

Similarly, we can obtain the pose of natural objects with circular or near-circular shape through the new efficient method:

$$\begin{cases} (\tilde{n}_{cir})_{new} = [0.8412, -0.4886, 0.2317]^T \\ \left(\tilde{O}_o\right)_{new} = [1002.1, 431.5, -224.4]^T\ (mm) \end{cases}$$
(57)

Define the error of the normal vector is $\delta\theta = \angle(\vec{n}_{real}, \vec{n}_{actual})$, compared with the conversion results of laser tracker, the traditional measurement error can be expressed as:

$$\begin{cases} \delta\theta_{old} = \angle\left(n_{cir}, (\tilde{n}_{cir})_{old}\right) = 2.1910° \\ \delta p_{old} = O_o - \left(\tilde{O}_o\right)_{old} \\ \qquad = \begin{bmatrix} 4.0172 & -4.8638 & 1.2784 \end{bmatrix}^T\ (mm) \end{cases}$$
(58)

Meanwhile, the new efficient measurement error can be obtained as:

$$\begin{cases} \delta\theta_{new} = \angle\left(n_{cir}, (\tilde{n}_{cir})_{new}\right) = 1.8073° \\ \delta p_{new} = O_o - \left(\tilde{O}_o\right)_{new} \\ \qquad = \begin{bmatrix} -1.9122 & 1.3653 & -1.8193 \end{bmatrix}^T\ (mm) \end{cases}$$
(59)

In order to better illustrate the effectiveness of the measurement method, in this paper, we selected two measurement targets on the satellite. As Fig. 23 shows, the two measured
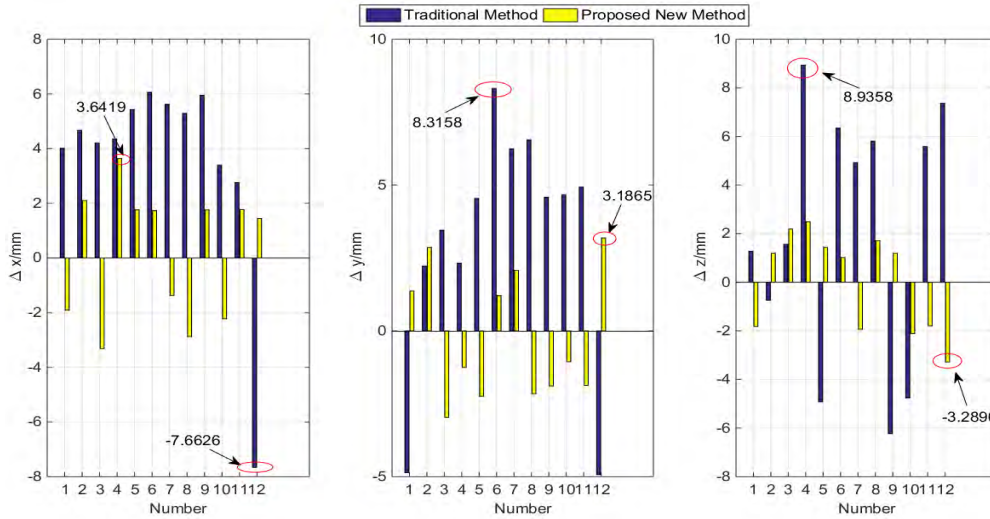
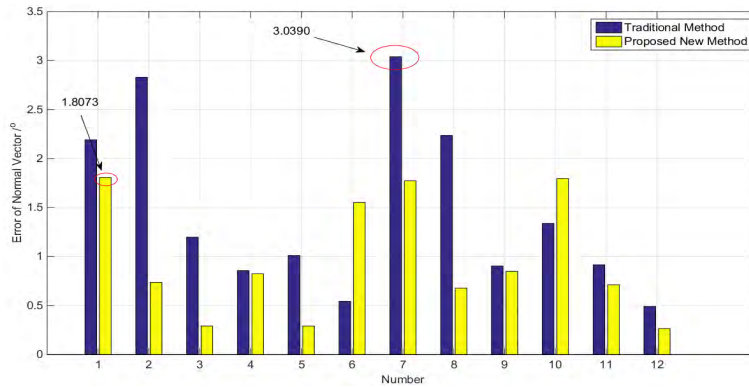**FIGURE 28.** The statistics error along with the *xyz*-axis.

FIGURE 29. The angle between the actual normal vector and the measured vector.

positions are symmetrically to the solar panel plane. Each group of experiments are collected a total of 12 sets of experimental data, in the first group of experiments, the statistical results of the actual value measured by the mentioned measurement method and FARO Laser Tracker measured results are shown in TABLE 2.

The position error of the traditional analytic method and the new efficient method on the *xyz*-axis are shown in Fig. 28, correspondingly, the angle between the actual normal vector and the real value is shown Fig. 29.

The statistical results show that the mean value of the position error of the traditional analytic method and new efficient method on the *xyz*-axis are $\bar{p}_{old}^1 = [4.9526, 4.8040, 4.8726]^T$ and $\bar{p}_{new}^1 = [2.1601, 2.0120, 1.8492]^T$ (mm), respectively; meanwhile, the average angle between the actual normal vector and the true value are $\bar{\theta}_{old}^1 = 1.4624°$ and $\bar{\theta}_{new}^1 = 0.9641°$, respectively.

We can see that the average angle of the position measurement accuracy is 58.76% higher than that of the traditional analytic method, and the accuracy of the normal vector is improved by 34.08%.

Another group of experiments also collected 12 sets of experimental data, the statistical results of the actual value measured by the mentioned visual measurement method and FARO Laser Tracker measured results are shown in TABLE 3.

Similarly, the position error of the traditional analytic method on the *xyz*-axis is shown in Fig. 30, the angle between the normal vector and the real value is shown Fig. 31.

The mean value of the position error of the traditional analytic method and new efficient method on the *xyz*-axis are $\bar{p}_{old}^2 = [4.6315, 4.1350, 3.8530]^T$ and $\bar{p}_{new}^2 = [3.7422, 2.7990, 3.0074]^T$ (mm), respectively; the average angle between the normal vector and the true value are $\bar{\theta}_{old}^2 = 1.3828°$ and $\bar{\theta}_{new}^2 = 0.8429°$, respectively. The average angle of position measurement accuracy is 23.95% higher than that of the traditional analytic method, and the accuracy of the normal vector is improved by 39.04%.

Given the extracted ellipse parameters $\{E_L, E_R\}$, the pose calculation platform is Windows7, and the processor is I3-4170. Calculate 12 groups of experimental data it takes an average of 0.0432s by the traditional analytical method,

TABLE 3. The pose error analysis table of the capture point 2.

| Name	Traditional analytic method of measurement error				The proposed new efficient` method of measurement error			
	Position error /mm			Normal vector deviation /º	Position error /mm			Normal vector deviation /º
	x^2_{old}	y^2_{old}	z^2_{old}	θ^2_{old}	x^2_{new}	y^2_{new}	z^2_{new}	θ^2_{new}
1	-4.4095	4.0967	5.5894	1.9962	1.6973	-5.1987	3.9271	1.5900
2	-5.6347	-5.0777	3.9703	1.8514	4.4748	2.4004	4.7655	0.6195
3	-4.9545	4.8935	1.1901	1.2554	3.3350	-2.3705	-3.0594	0.4477
4	-7.3948	5.9461	4.3616	0.2204	-1.2190	3.1991	-1.6252	0.2049
5	-5.4996	-5.6769	4.0226	1.9696	3.0139	2.2749	-2.3323	0.6336
6	-4.0000	3.6400	-3.8426	2.9002	4.0305	2.6335	-3.6320	1.3997
7	-5.0685	6.1788	-3.8307	0.2348	9.8160	1.3798	-5.0499	0.5125
8	3.2560	1.9946	-2.4223	1.2995	1.5848	1.5253	-2.9935	1.5510
9	-4.3291	4.5603	-7.9579	0.6065	3.1617	2.4821	3.7505	0.7135
10	-2.6385	4.1072	1.5978	0.5864	-6.5865	-3.7154	-1.7464	0.3330
11	5.5670	-1.5223	4.0750	1.6450	-3.7720	-1.7778	1.7373	1.0825
12	-2.8256	-1.9256	-3.3752	2.0275	-2.2152	4.6308	1.4695	1.0274
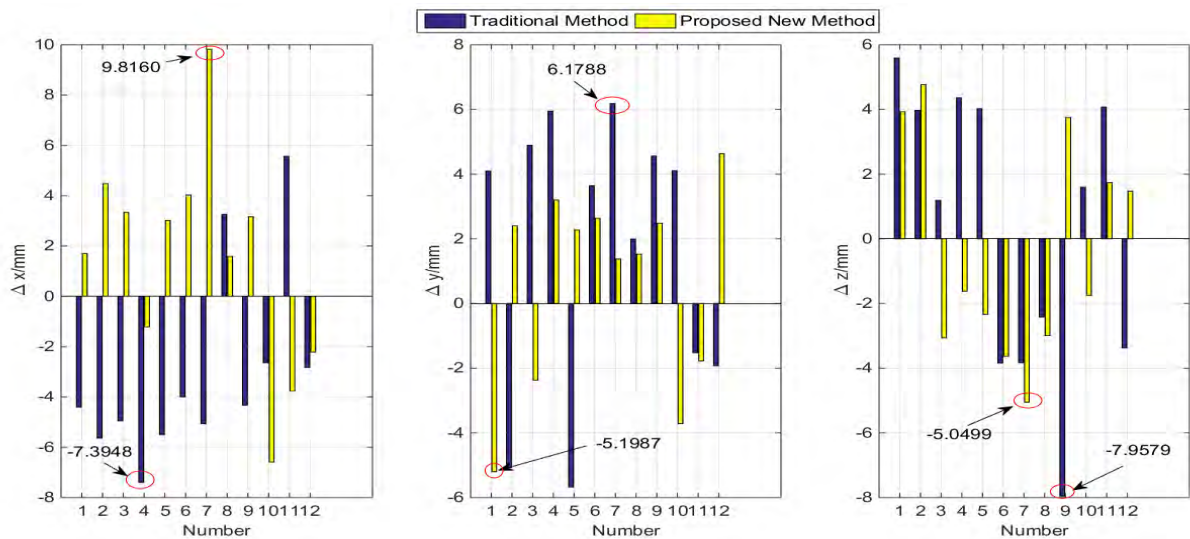
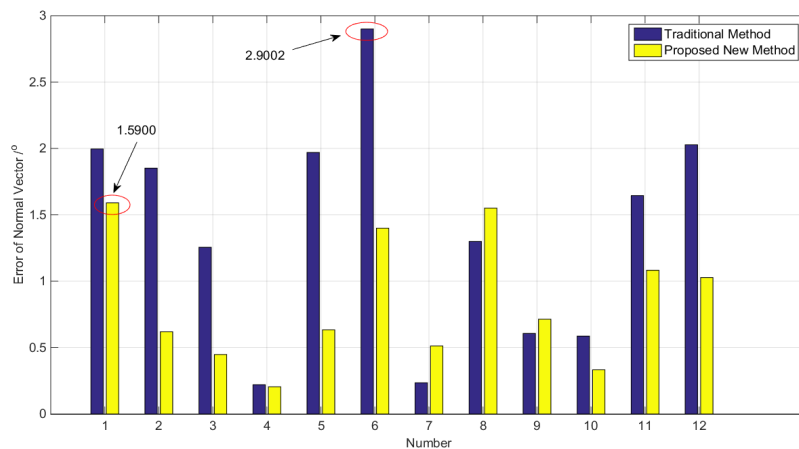**FIGURE 30.** The statistics error along with the *xyz* axis.

FIGURE 31. The angle between the actual normal vector and the measured vector.

however, when using the new efficient method to calculate the similar data, it only costs 0.0019s, which greatly reducing the time spent by pose calculation, therefore, it will contribute to the real-time performance of subsequent capturing the non-cooperative target. In view of the acceleration of image preprocessing, the efficiency of the new pose calculation

method is nearly 96% higher than that of the traditional method in the whole pose measurement process.

VI. CONCLUSIONS AND FUTURE WORK

Recognition and pose measurement of non-cooperative targets are very important for on-orbital servicing. Since non-cooperation target has not any cooperation logo or any prior knowledge, it is very difficult to measure the information of the target points based on vision. By analyzing the characteristics of the non-cooperative target, an efficient method to determine the pose of natural objects with circular or near-circular shape is proposed. In the process of static distance measurement, we can use the hand-eye camera co-measurement method to ensure the operation of visual measurement. Compared with the traditional method, the proposed method has higher accuracy and efficiency. Moreover, considering the pre-processing of visual measurement is very time-consuming, we realized the image pre-processing algorithms (including median filter, edge detection and the ellipse recognition) on the FPGAs, which has a strong parallel processing power. The proposed results are then transferred through USB interface to the MFC visual software to do post-processing. Hence, the image processing speed is further improved. The validity of the proposed method is verified by experiments.

An interesting work to be accomplished in the future is to make an exhaustive study of the optimal strategy for capturing the non-cooperative target. In addition, experiments with motion estimation could be useful to predict the movement of the non-cooperative target. Furthermore, how to optimize the visual measurement algorithm, further adoption of parallel computing to speed up the image algorithm is an important aspect of the future research.

REFERENCES

[1] M. Oda, "Space robot experiments on NASDA's ETS-VII satellite preliminary overview of the experiment results," in *Proc. IEEE Int. Conf. Robot. Autom.*, Detroit, MI, USA, May 1999, pp. 1390–1395.

[2] C. Elliott, O. Layi, R. Richard, B. Bardia, R. Daniel, and S. Shelley, "Dextre: Improving maintenance operations on the international space station," *Acta Astronautica*, vol. 64, nos. 9–10, pp. 869–874, 2009.

[3] M. Shan, J. Guo, and E. Gill, "Review and comparison of active space debris capturing and removal methods," *Prog. Aerosp. Sci.*, vol. 80, pp. 18–32, Jan. 2016.

[4] A. Flores-Abad, O. Ma, K. Pham, and S. Ulrich, "A review of space robotics technologies for on-orbit servicing," *Prog. Aerosp. Sci.*, vol. 68, pp. 1–26, Jul. 2014.

[5] P. Huang, F. Zhang, J. Cai, D. Wang, Z. Meng, and J. Guo, "Dexterous tethered space robot: Design, measurement, control, and experiment," *IEEE Trans. Aerosp. Electron. Syst.*, vol. 53, no. 3, pp. 1452–1468, Jun. 2017.

[6] T. Yasaka and E. W. Ashford, "GSV: An approach toward space system servicing," *Earth Space Rev.*, vol. 5, no. 2, pp. 9–17, 1996.

[7] J. K. Thienel, J. M. Van Eepoel, and R. M. Sanner, "Accurate state estimation and tracking of a non-cooperative target vehicle," in *Proc. AIAA Guid., Navigat., Control Conf.*, Keystone, CO, USA, 2006, pp. 5511–5522.

[8] X. Du, B. Liang, W. Xu, and Y. Qiu, "Pose measurement of large non-cooperative satellite based on collaborative cameras," *Acta Astronautica*, no. 68, nos. 11–12, pp. 2047–2065, 2011.

[9] S. J. Zhang, X. B. Cao, and M. Chen, "Monocular vision-based relative pose parameters determination for non-cooperative spacecrafts," *J. Nanjing Univ. Sci. Technol.*, vol. 30, no. 5, pp. 564–568, 2006.

[10] N. Inaba, M. Oda, and M. Asano, "Rescuing a stranded satellite in space-experimental robotic capture of non-cooperative satellites," *Trans. Jpn. Soc. Aeronautical Space Sci.*, vol. 48, no. 162, pp. 213–220, 2016.

[11] M. D. Lichter and S. Dubowsky, "State, shape, and parameter estimation of space objects from range images," in *Proc. IEEE Int. Conf. Robot. Autom.*, vol. 3. Apr./May 2004, pp. 2974–2979.

[12] P. Jasiobedski, M. Greenspan, and G. Roth, "Pose determination and tracking for autonomous satellite capture," in *Proc. Int. Symp. Artif. Intell., Robotics Autom. Space*, 2001, pp. 1–9.

[13] F. Terui, H. Kamimura, and S. Nishida, "Motion estimation to a failed satellite on orbit using stereo vision and 3D model matching," in *Proc. Int. Conf. Control, Autom., Robot. Vis.*, Dec. 2006, pp. 1–8.

[14] X. Gao , K. Xu , H. Zhang, and X. Liu, "Position-pose measurement algorithm based on single camera and laser range-finder," *J. Sci. Instrum.*, vol. 28, no. 8, pp. 1479–1485, 2007.

[15] G. Hirzinger *et al.*, "DLR's robotics technologies for on-orbit servicing," *Adv. Robot.*, vol. 18, no. 2, pp. 139–174, 2004.

[16] K. Landzettel. (2008). *Technology Satellite for Demonstration and Verification of Space Systems*. [Online]. Available: http://www.robotic. dlr.de/TECSAS

[17] T. J. Debus and S. P. Dougherty, "Overview and performance of the front-end robotics enabling near-term demonstration (FREND) robotic arm," in *Proc. AIAA Infotech Aerosp. Conf.*, Washington, DC, USA, 2009, pp. 1–12.

[18] J. A. Lennon and C. G. Henshaw, "An architecture for autonomous control of a robotic satellite grappling mission," in *Proc. AIAA Guid., Navigat. Control Conf. Exhibit*, Honolulu, HI, USA, 2008, pp. 1–8.

[19] J. Obermark, G. Creamer, B. E. Kelm, W. Wagner, and C. G. Henshaw, "SUMO/FREND: Vision system for autonomous satellite grapple," *Proc. SPIE*, vol. 6555, pp. 65550Y-1–65550Y-11, May 2007.

[20] R. Li, Y. Zhou, F. Chen, and Y. Chen, "Parallel vision-based pose estimation for non-cooperative spacecraft," *Adv. Mech. Eng.*, vol. 7, no. 7, pp. 1–9, 2015.

[21] L. Zhang, S. Zhang, H. Yang, H. Cai, and S. Qian, "Relative attitude and position estimation for a tumbling spacecraft," *Aerosp. Sci. Technol.*, vol. 42, pp. 97–105, Apr./May 2015.

[22] L. Sun and W. Huo, "Robust adaptive relative position tracking and attitude synchronization for spacecraft rendezvous," *Aerosp. Sci. Technol.*, vol. 41, pp. 28–35, Feb. 2015.

[23] B. E. Tweddle, A. Saenz-Otero, J. J. Leonard, and D. W. Miller, "Factor graph modeling of rigid-body dynamics for localization, mapping, and parameter estimation of a spinning object in space," *J. Field Robot.*, vol. 32, no. 6, pp. 897–933, 2015.

[24] G. Dong and Z. H. Zhu, "Vision-based pose and motion estimation of non-cooperative target for space robotic manipulators," in *Proc. AIAA SPACE Conf. Expo.*, San Diego, CA, USA, Aug. 2014.

[25] J. Kaiser, A. Martinelli, F. Fontana, and D. Scaramuzza, "Simultaneous state initialization and gyroscope bias calibration in visual inertial aided navigation," *IEEE Trans. Robot. Autom. Lett.*, vol. 2, no. 1, pp. 18–25, Jan. 2017.

[26] G. Dong and Z. H. Zhu, "Autonomous robotic capture of non-cooperative target by vision-based kinematic control," in *Proc. AIAA SPACE Conf. Expo.*, Pasadena, CA, USA, Aug. 2015, pp. 157–167.

[27] R. Safaee-Rad, I. Tchoukanov, K. C. Smith, and B. Benhabib, "Three-dimensional location estimation of circular features for machine vision," *IEEE Trans. Robot. Autom.*, vol. 8, no. 5, pp. 624–640, Oct. 1992.

[28] R. Y. Tsai and R. K. Lenz, "A new technique for fully autonomous and efficient 3D robotics hand/eye calibration," *IEEE Trans. Robot. Autom.*, vol. 5, no. 3, pp. 345–358, Jun. 1989.

[29] Q. Ma, H. Li, and G. S. Chirikjian, "New probabilistic approaches to the AX = XB hand-eye calibration without correspondence," in *Proc. IEEE Int. Conf. Robot. Autom.*, May 2016, pp. 4365–4371.

[30] R. Thomas, P. Tomas, and K. Lars, "Globally optimal hand-eye calibration," in *Proc. IEEE Conf. Comput. Vis. Pattern Recognit. (CVPR)*, Providence, RI, USA, Jun. 2012, pp. 1035–1042.

[31] H. Jan, H. Michal, and P. Tomas, "Globally optimal hand-eye calibration using branch-and-bound," *IEEE Trans. Pattern Anal. Mach. Intell.*, vol. 38, no. 5, pp. 1027–1033, May 2016.

[32] Z. J. Zhao, "Hand-eye calibration using convex optimization," in *Proc. IEEE Int. Conf. Robot. Autom.*, May 2011, pp. 2947–2952.

[33] F. Liu, J. Li, H. Wang, and C. Liu, "An improved quaternion Gauss–Newton algorithm for attitude determination using magnetometer and accelerometer," *Chin. J. Aeronautics*, vol. 27, no. 4, pp. 986–993, 2014.

[34] Z. Chen and J.-B. Huang, "A vision-based method for the circle pose determination with a direct geometric interpretation," *IEEE Trans. Robot. Autom.*, vol. 15, no. 6, pp. 1135–1140, Dec. 1999.

[35] W. Xu, Q. Xue, H. Liu, X. Du, and B. Liang, "A pose measurement method of a non-cooperative GEO spacecraft based on stereo vision," in *Proc. 12th Int. Conf. Control Autom. Robot. Vis. (ICARCV)*, Guangzhou, China, Dec. 2012, pp. 966–971.
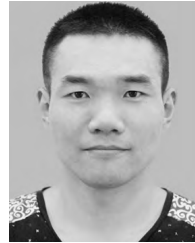
WENFU XU (M'13–SM'16) received the B.E. and M.E. degrees in control engineering, from the Hefei University of Technology, Hefei, China, in 2001 and 2003, respectively, and the Ph.D. degree in control science and engineering from the Harbin Institute of Technology, Harbin, China, in 2007. He was a Research Associate with the Department of Mechanical and Automation Engineering, The Chinese University of Hong Kong, Hong Kong.

He is currently a Professor with Harbin Institute of Technology Shenzhen Graduate School, Shenzhen, China. His research interests include space robotics, multi-body system dynamic, and redundant manipulator.

JIANQING PENG received the B.E. degree in mechatronics engineering from Huazhong Agricultural University, Wuhan, China, in 2012, and the M.E. degree in mechatronics engineering from Harbin Institute of Technology, Shenzhen, China, in 2014.

He is currently pursuing the Ph.D. degree with the Department of Mechatronics and Automation, Harbin Institute of Technology, Shenzhen, China. His research interests include space robotics, computer vision, SLAM, image processing, and FPGA.

HAN YUAN received the Ph.D. degree in mechanical engineering from the Institut National des Sciences Appliquées de Rennes, Rennes, France, in 2015. He was a Research Scientist with CNRS UMR6602, Clermont-Ferrand, France, from 2015 to 2016, and a Post-Doctoral Fellow with The Chinese University of Hong Kong, Hong Kong, China, from 2016 to 2017.

He is currently an Assistant Professor with Harbin Institute of Technology Shenzhen Graduate School, Shenzhen, China. His research interests include computer vision, cable-driven manipulators, and flexible actuators.

• • •